Chapter 3: Observations: Surface and Atmospheric Climate Change
Figures

Coordinating Lead Authors: Kevin E. Trenberth (USA), Philip D. Jones (UK)

Lead Authors: Peter G. Ambenje (Kenya), Roxana Bojariu (Romania), David R. Easterling (USA), Albert M. G. Klein Tank (The Netherlands), David E. Parker (UK), James A. Renwick (New Zealand), Fatemeh Rahimzadeh (Iran), Matilde M. Rusticucci (Argentina), Brian J. Soden (USA), Pan-Mao Zhai (China)

Contributing Authors: Robert Adler (USA), Lisa Alexander (UK, Australia, Ireland), Hans Alexandersson (Sweden), Richard P. Allan (UK), Mark P. Baldwin (USA), Martin Beniston (Switzerland), David H. Bromwich (USA), Inés Camilloni (Argentina), Christophe Cassou (France), Daniel R. Cayan (USA), Edmund K. M. Chang (USA), John R. Christy (USA), Aiguo Dai (USA), Clara Deser (USA), Nikolai Dotzek (Germany), John Fasullo (USA), Ryan L. Fogt (USA), Christopher K. Folland (UK), Piers Forster (UK), Melissa Free (USA), Christoph Frei (Switzerland), Byron Gleason (USA), Jürgen Grieser (Germany), Pavel Y. Groisman (USA), Sergey K. Gulev (Russia), James W. Hurrell (USA), Masayoshi Ishii (Japan), Simon A. Josey (UK), Per W. Kållberg (ECMWF), John Kennedy (UK), George N. Kiladis (USA), Ramesh H. Kripalani (India), Kenneth E. Kunkel (USA), Chiu Ying Lam (China), John R. Lanzante (USA), Jay H. Lawrimore (USA), David H. Levinson (USA), Beate G. Liepert (USA), Gareth J. Marshall (UK), Carl A. Mears (USA), Philip W. Mote (USA), Hishashi Nakamura (Japan), Neville Nicholls (Australia), Joel R. Norris (USA), Taikan Oki (Japan), Franklin R. Robertson (USA), Karen H. Rosenlof (USA), Fred H. Semazzi (USA), Dennis J. Shea (USA), J. Marshall Shepherd (USA), Theodore G. Shepherd (Canada), Steven. C. Sherwood (USA), Adrian J. Simmons (ECMWF, UK), Ian Simmonds (Australia), Peter C. Siegmund (The Netherlands), Chris D. Thorncroft (USA), Peter W. Thorne (UK), Sakari M. Uppala (ECMWF), Russell S. Vose (USA), Bin Wang (USA), Stephen G. Warren (USA), Richard Washington (UK, South Africa), Matthew C. Wheeler (Australia), Bruce A. Wielicki (USA), Takmeng Wong (USA), David B. Wuertz (USA)

Review Editors: Brian J. Hoskins (UK), Bubu Pateh Jallow (The Gambia), Thomas R. Karl (USA)

Date of Draft: 27 October 2006

Figures

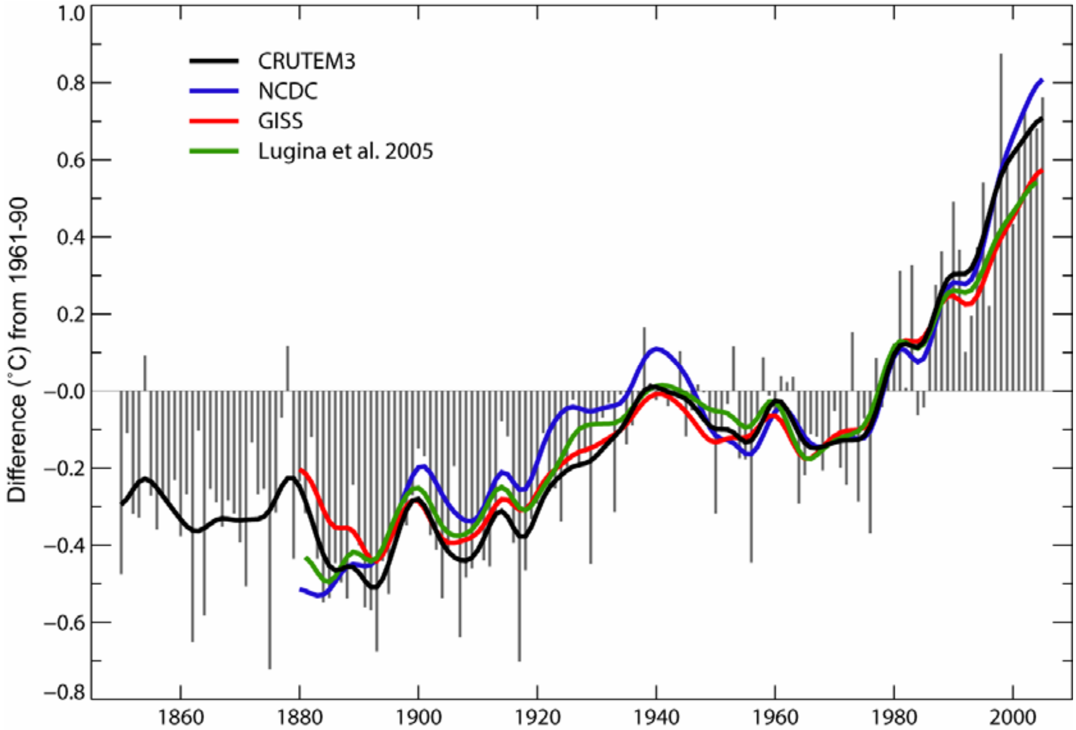

Figure 3.1. Annual anomalies of global land surface air temperature (°C), 1850 to 2005, relative to the 1961–1990 mean for CRUTEM3 updated from Brohan et al. (2006). The smooth curves depict decadal-filtered variations (see Appendix 3.A). The thick solid black curve from CRUTEM3 is compared with those from NCDC (Smith and Reynolds, 2005) (blue) and GISS (Hansen et al., 2001) (red) and Lugina et al. (2005) (green).

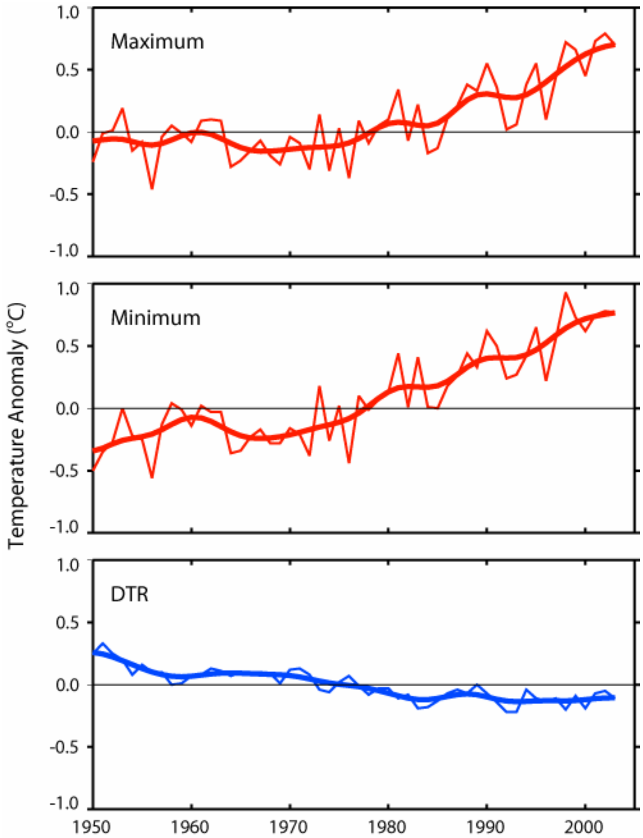

Figure 3.2. Annual anomalies relative to the 1961 to 1990 mean of maximum and minimum temperatures and diurnal temperature range (DTR) (°C) averaged for the 71% of global land areas where data are available for 1950 to 2004. The smoothed curve shows the decadal variability (Appendix 3.A). Adapted from Vose et al. (2005a).

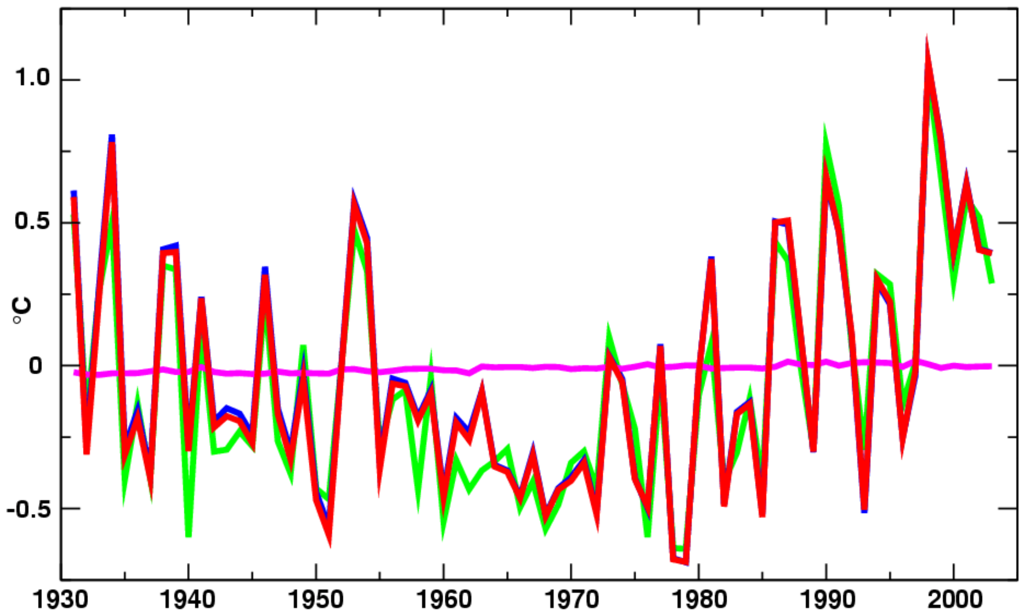

Figure 3.3. Anomaly (°C) time series relative to the 1961 to 1990 mean of the full USHCN data (red), the USHCN data without the 16% of the stations with populations of over 30,000 within 6 km in the year 2000 (blue), and the 16% of the stations with populations over 30,000 (green). The full USHCN set minus the set without the most urban stations is shown in magenta. Both the full data set and the data set without the high population stations had stations in all of the 2.5° latitude by 3.5° longitude grid boxes during the entire period plotted but the subset of high population stations only had data in 56% of these grid boxes.

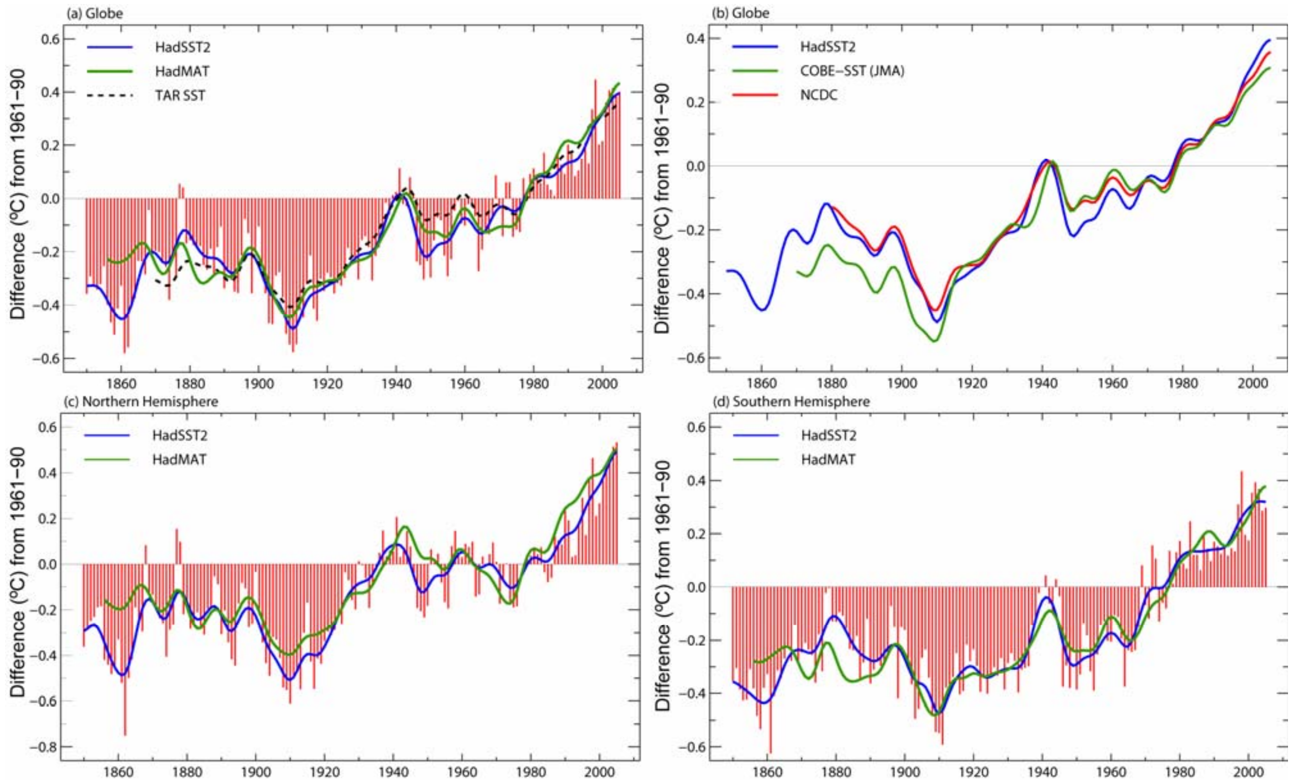

Figure 3.4. Annual anomalies of global SST (HadSST2; red bars and blue solid curve), 1850 to 2005, and global night marine air temperature (HadMAT, green curve), 1856 to 2005, relative to the 1961–1990 mean (°C) from UKMO (Rayner et al., 2006). The 13-point decadal filter (Appendix 3.A) provides the smoothed curves. The dashed black curve shows equivalent smoothed SST anomalies from the TAR. (b) Smoothed annual global SST anomalies, relative to 1961 to 1990 (°C), from HadSST2 (blue line, as in a)), from Smith et al. (2005) (NCDC; red line), and from Japan [(Ishii et al., 2005) COBE-SST (JMA), green line]. These latter two series begin later in the 19th century than HadSST2. (c, d) as in (a) but for the NH and SH showing only the UKMO (Rayner et al., 2006) series.

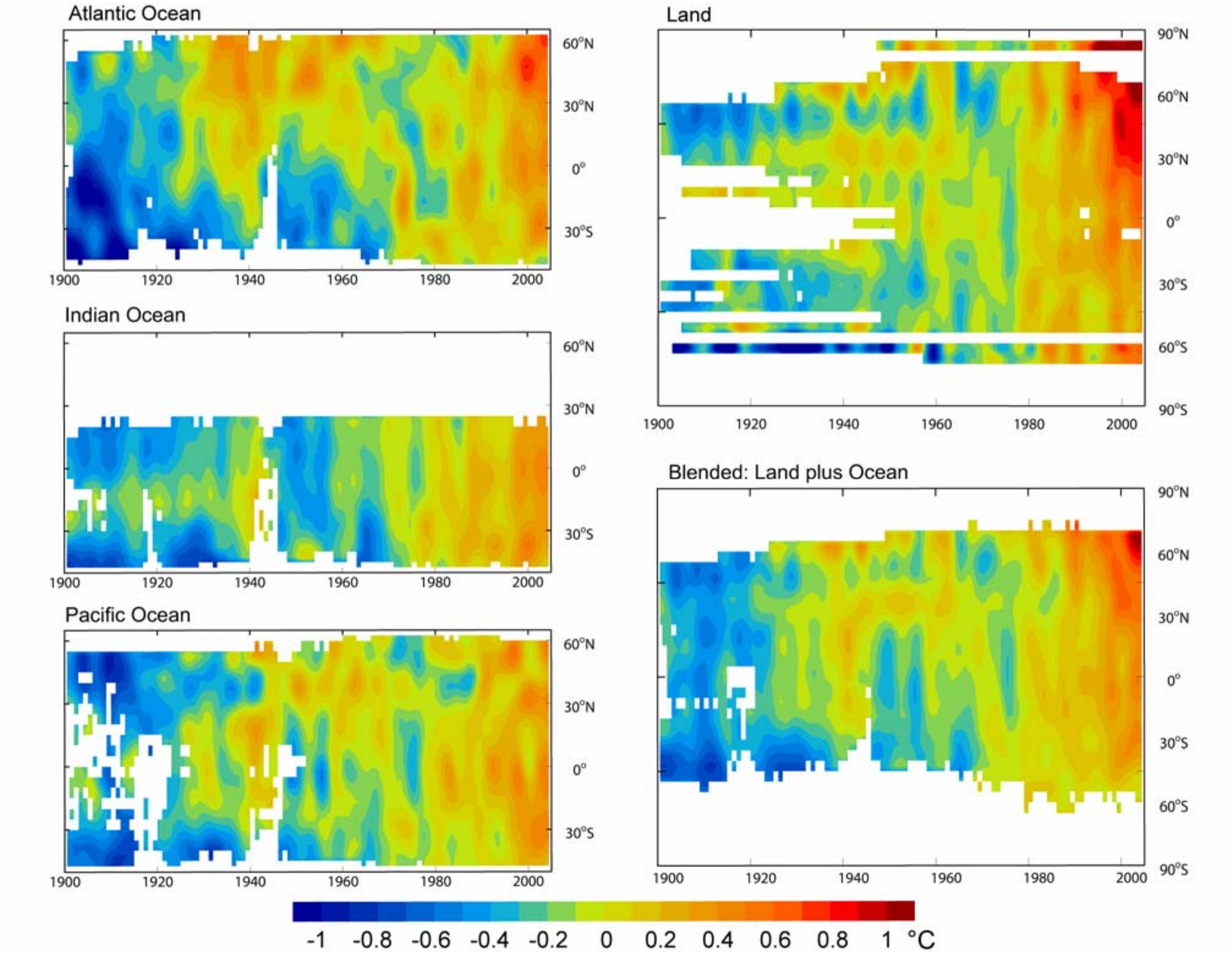

Figure 3.5. Latitude-time sections of zonal mean temperature anomalies (°C) from 1900 to 2005, relative to the 1961 to 1990 mean. Left panels: SST annual anomalies across each ocean from HadSST2 (Rayner et al., 2006). Right panels: Surface temperature annual anomalies for land (top, CRUTEM3) and land plus ocean (bottom, HadCRUT3). The values are smoothed with a 1/12(1–3–4–3–1) filter to remove fluctuations less than 6 years or so (see Appendix 3.A) and missing data are white.

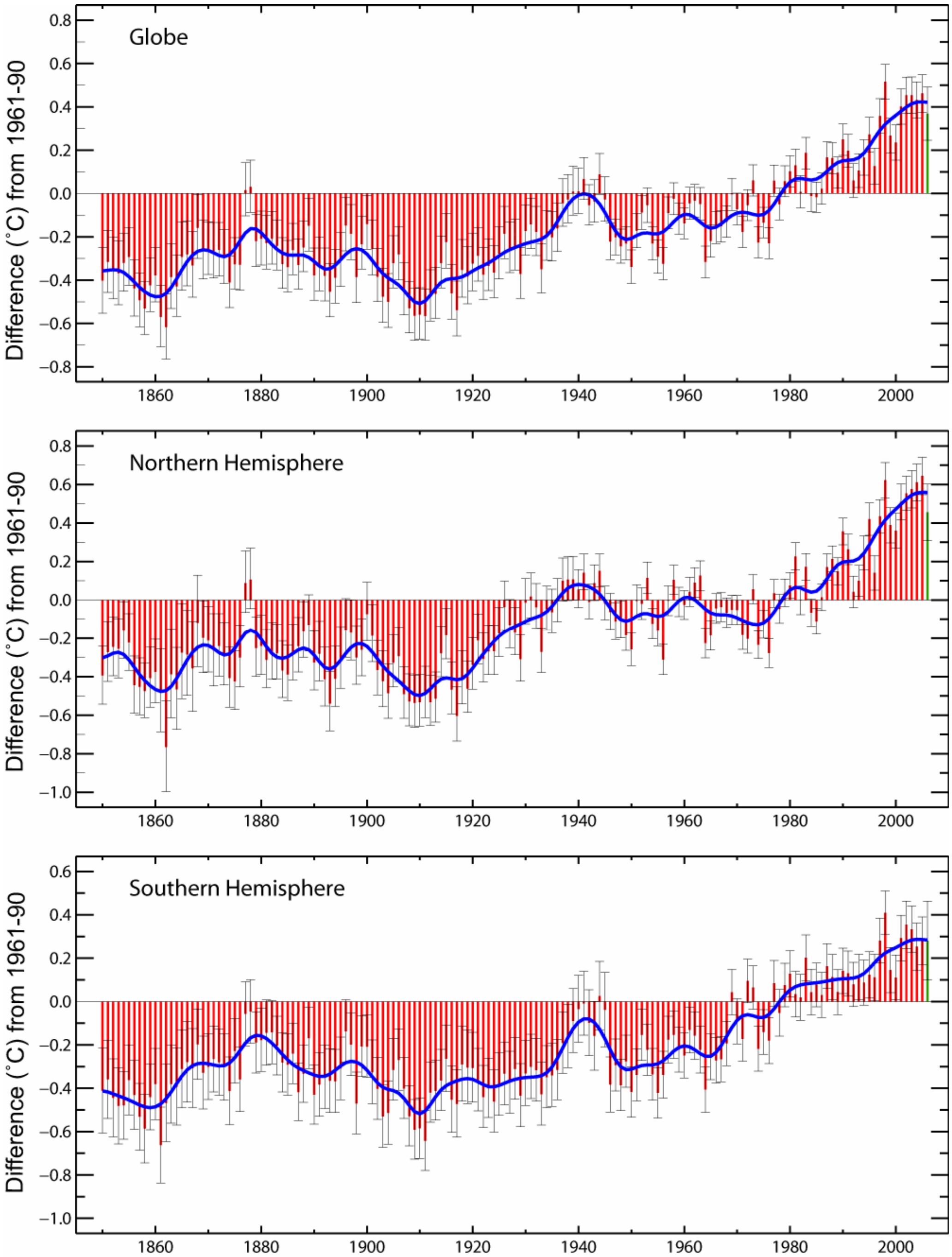

Figure 3.6. Global and hemispheric annual combined land surface air temperature and SST anomalies (°C) (red) relative to the 1961 to 1990 mean, along with 5 to 95% error bar ranges, from HadCRUT3 (adapted from Brohan et al., 2006). The blue decadal smoothing is described in Appendix 3.A. The preliminary value for 2006 is given as a green bar.

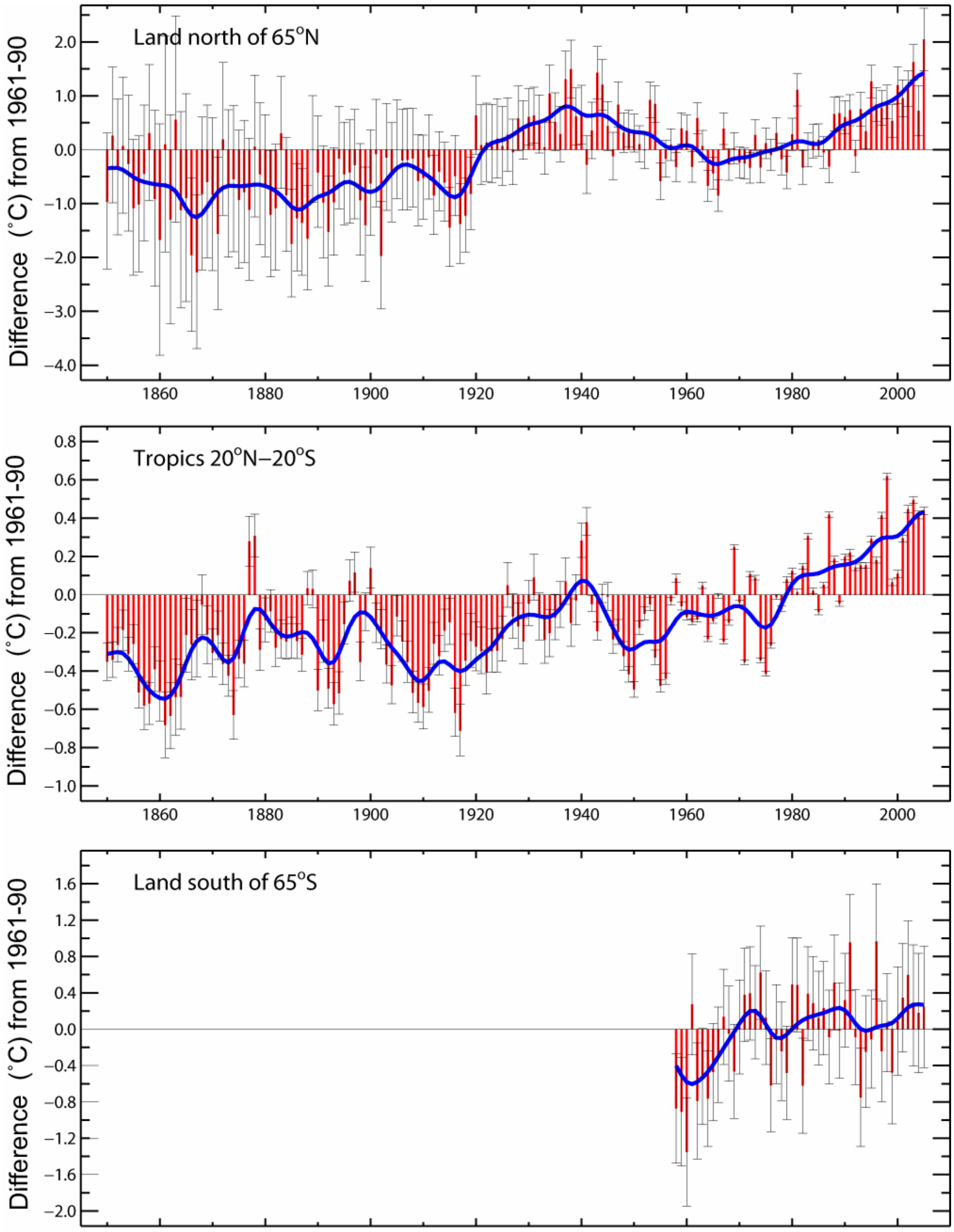

Figure 3.7. Annual temperature anomalies (°C), relative to the 1961 to 1990 mean. The tropical series is combined land surface air temperature and SST from HADCRUT3 (adapted from Brohan et al., 2006). The polar series are land-only from CRUTEM3 because SST data are sparse and unreliable in sea-ice zones. Blue decadal smoothing is described in Appendix 3.A and 5 to 95% error bars are shown.

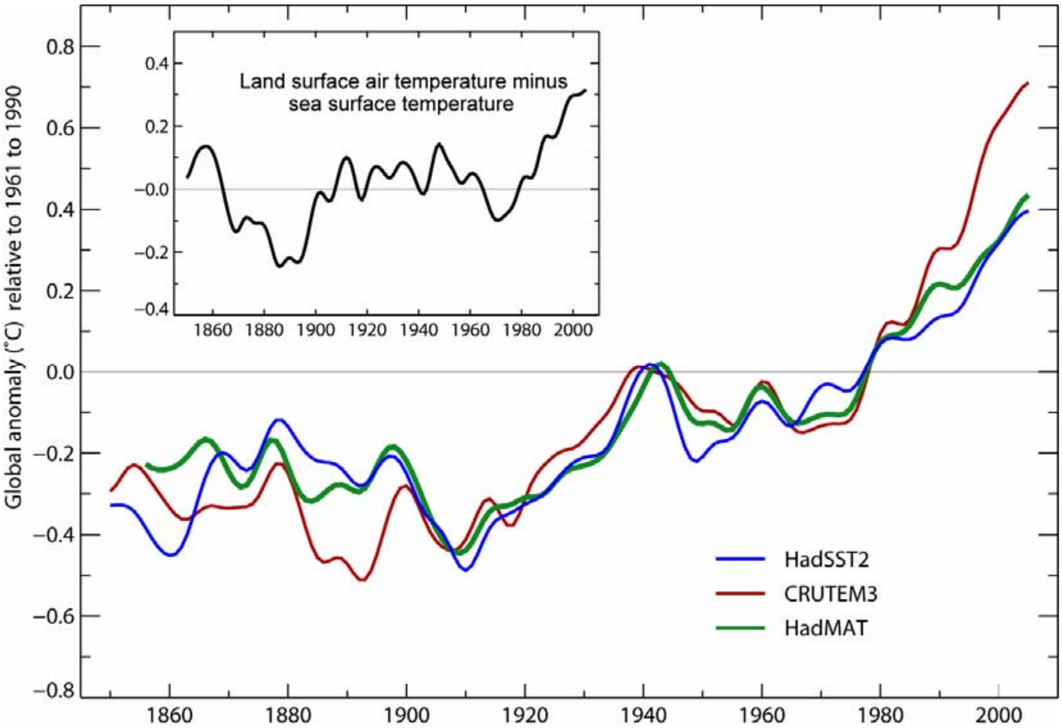

Figure 3.8. Decadally-smoothed (Appendix 3.A) annual anomalies of global average SST (blue curve, begins 1850), night marine air temperature (green curve, begins 1856) and land surface air temperature (red curve, begins 1850) to 2005, relative to their 1961 to 1990 means (°C) (Rayner et al., 2006; Brohan et al., 2006). Also shown (inset) are the smoothed differences between the land-surface air and SST anomalies (i.e., red minus blue).

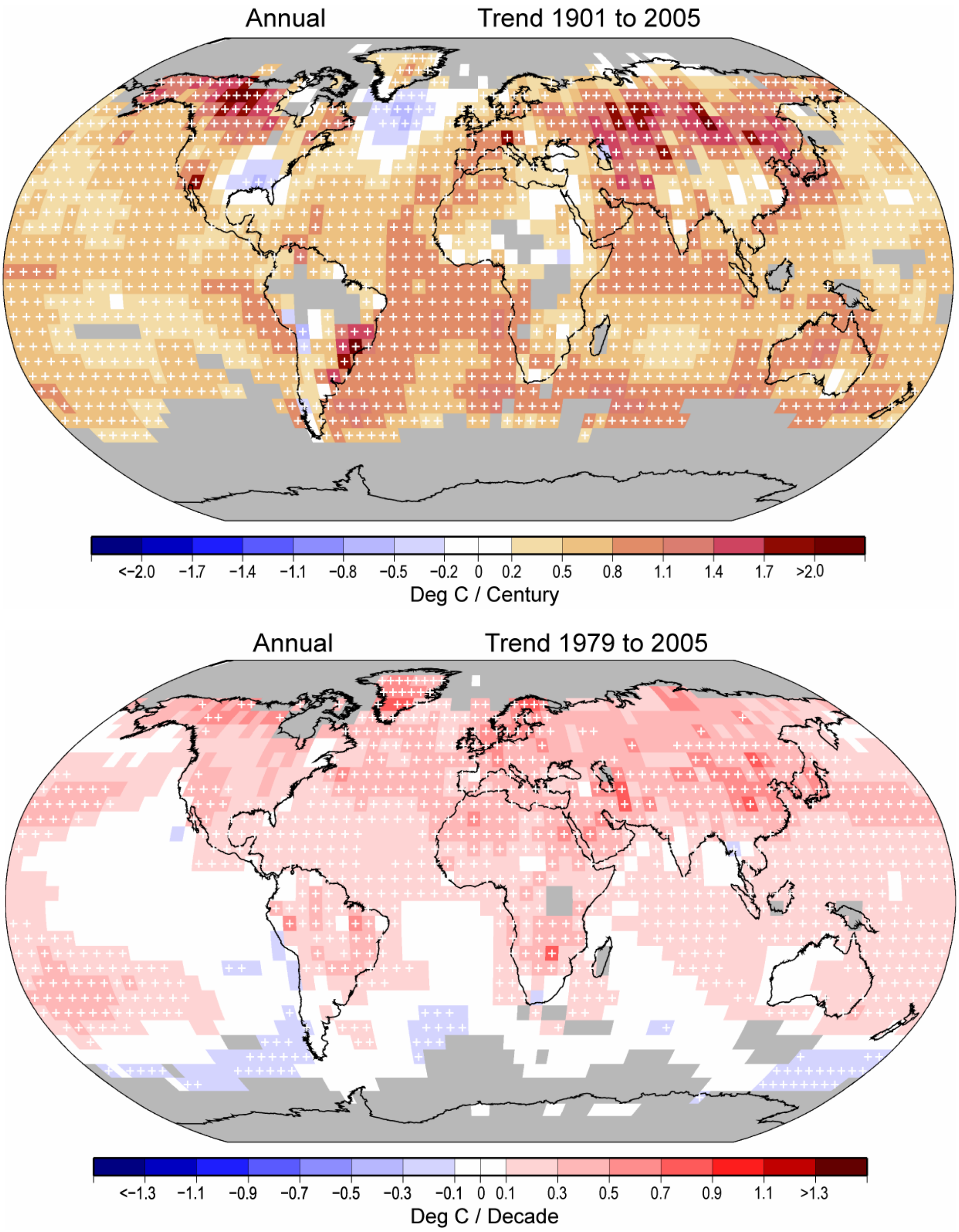

Figure 3.9. Linear trend of annual temperatures for 1901 to 2005 (upper; °C century^{-1}) and 1979 to 2005 (lower; °C decade^{-1}). Areas in grey have insufficient data to produce reliable trends. The minimum number of years needed to calculate a trend value is 66 years for 1901 to 2005 and 18 years for 1979 to 2005. An annual value is available if there are 10 valid monthly temperature anomaly values. The dataset used was produced by NCDC from Smith and Reynolds (2005). Trends significant at the 5% level are indicated by white + marks.

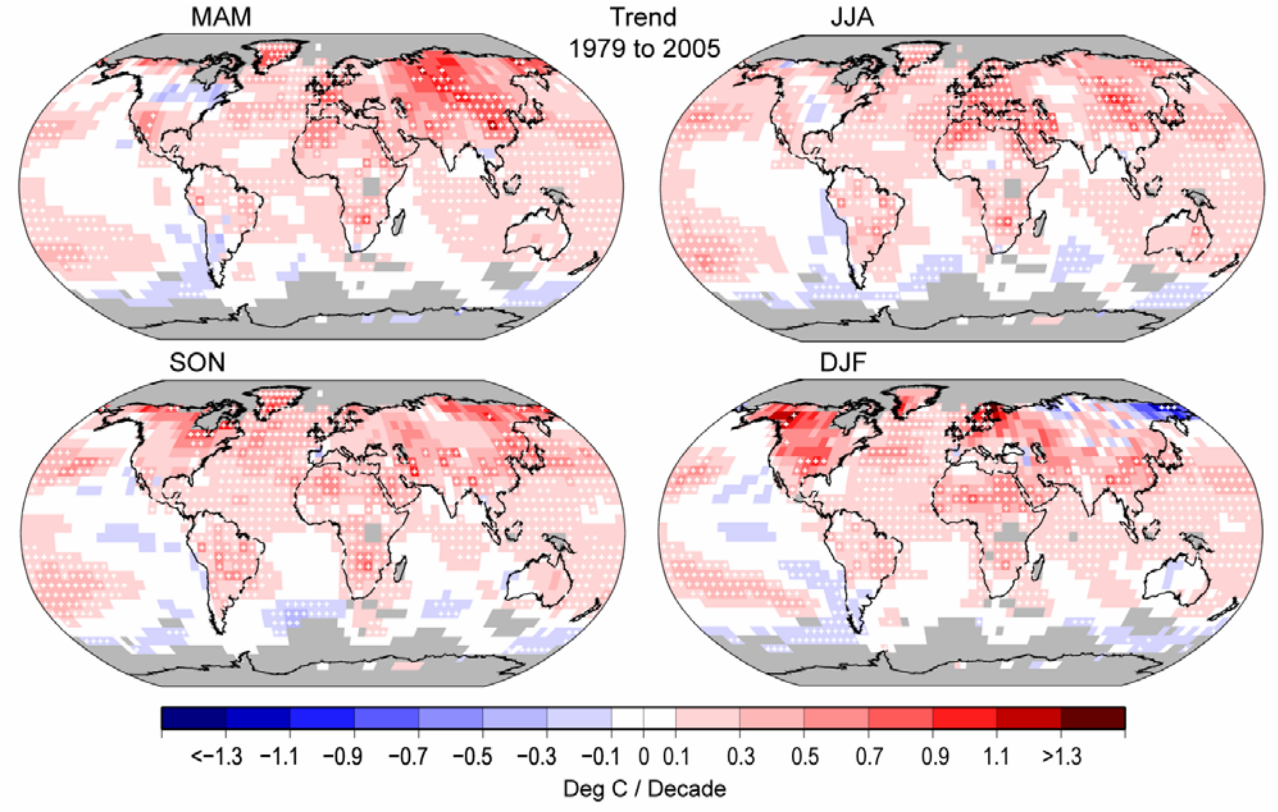

Figure 3.10. Linear trend of seasonal MAM, JJA, SON and DJF temperature for 1979 to 2005. The units are °C decade^{-1}. Areas in grey have insufficient data to produce reliable trends. The minimum number of years to calculate a trend value is 18. A seasonal value is available if there are 2 valid monthly temperature anomaly values. The dataset used was produced by NCDC from Smith and Reynolds (2005). Trends significant at the 5% level are indicated by white + marks.

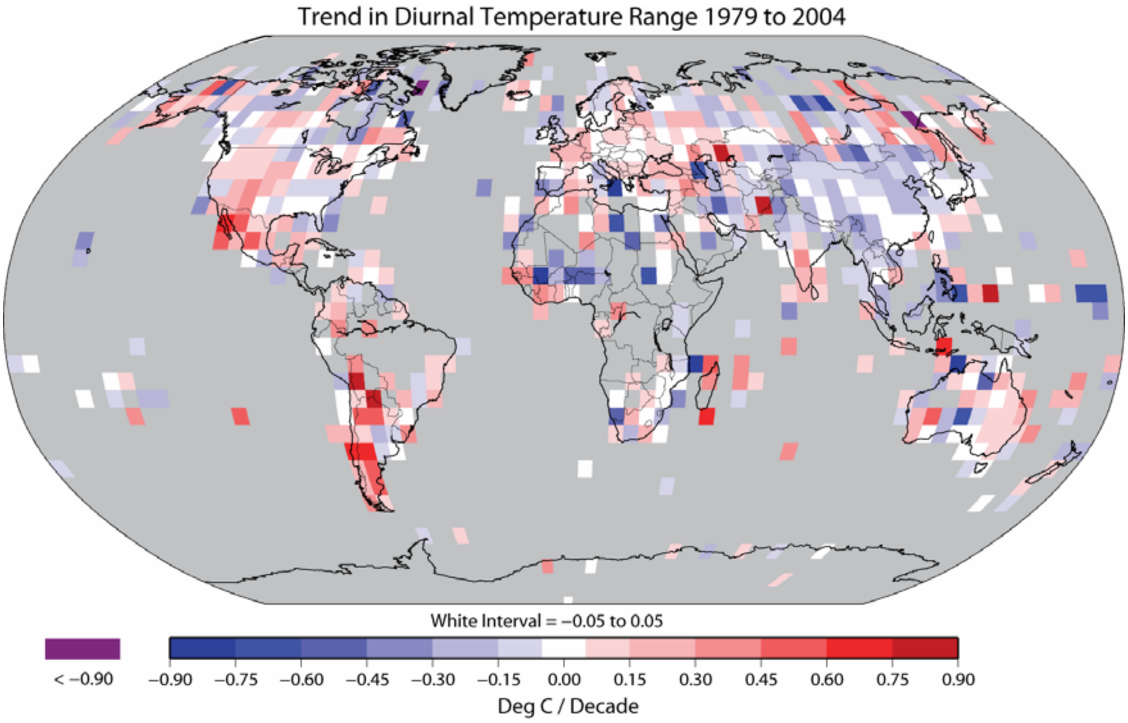

Figure 3.11. Linear trend in annual mean DTR for 1979 to 2004 in °C decade^{-1}. Grey regions indicate incomplete or missing data. After Vose et al. (2005a).

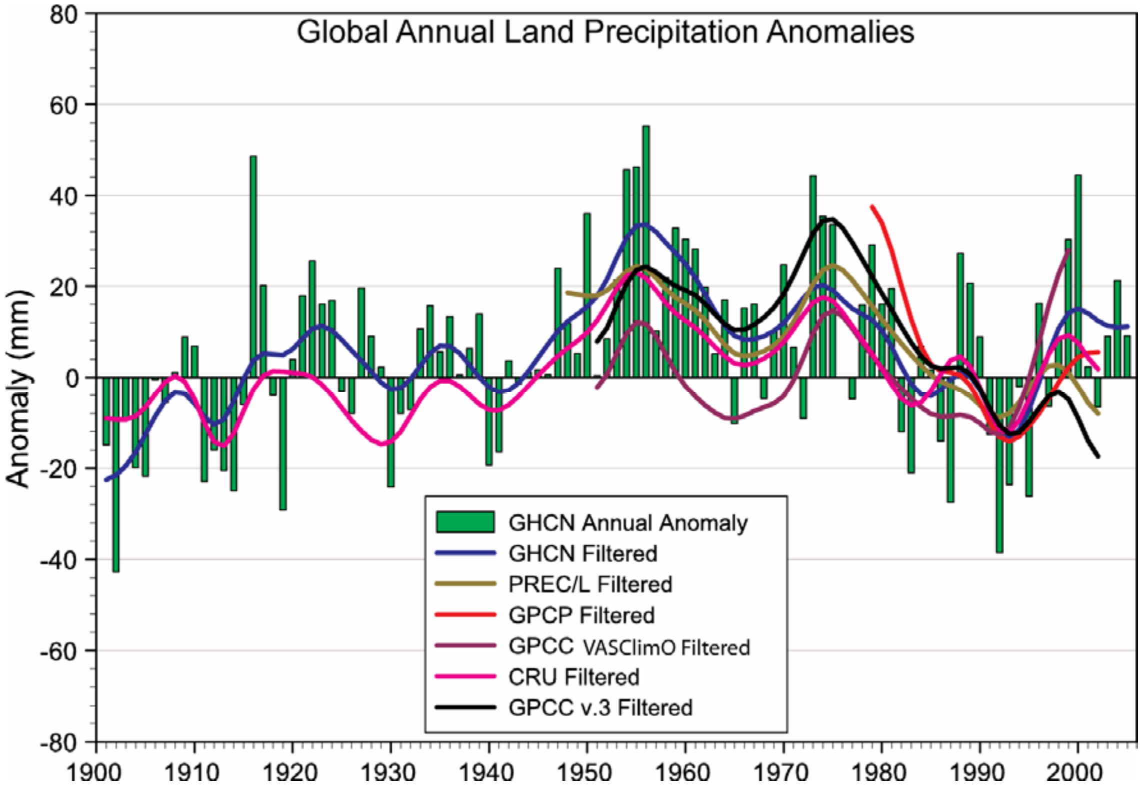

Figure 3.12. Time series for 1900 to 2005 of annual global land precipitation anomalies (mm) from GHCN with respect to the 1981–2000 base period. Smoothed values (using the decadal filter in Appendix 3.A) are also given for the GHCN (Peterson and Vose, 1997), PREC/L (Chen et al. (2002)), GPCP (Adler et al., 2003), GPCC (Rudolf et al., 1994) and CRU (Mitchell and Jones, 2005).

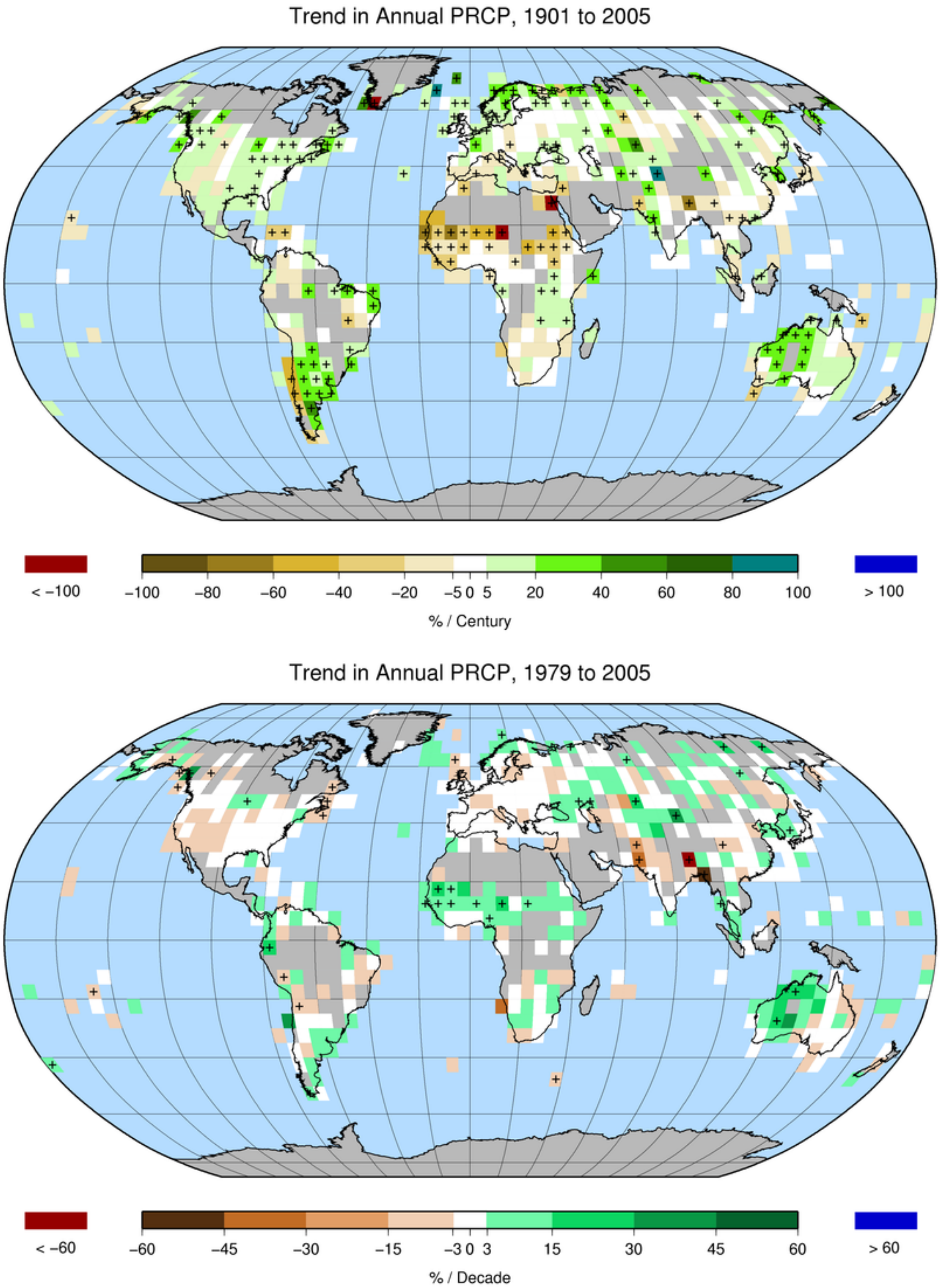

Figure 3.13. Trend of annual precipitation amounts for 1901 to 2005 (upper, % century^{-1}) and 1979 to 2005 (lower, % decade^{-1}) the percentage being based on the 1961 to 1990 period. Areas in grey have insufficient data to produce reliable trends. The minimum number of years to calculate a trend value is 66 for 1901 to 2005 and 18 for 1979 to 2005. An annual value is complete for a given year if all twelve monthly percentage anomaly values are present. The GHCN precipitation dataset from NCDC was used. Note the different colour bars and units in each plot. Trends significant at the 5% level are indicated by black + marks.

.

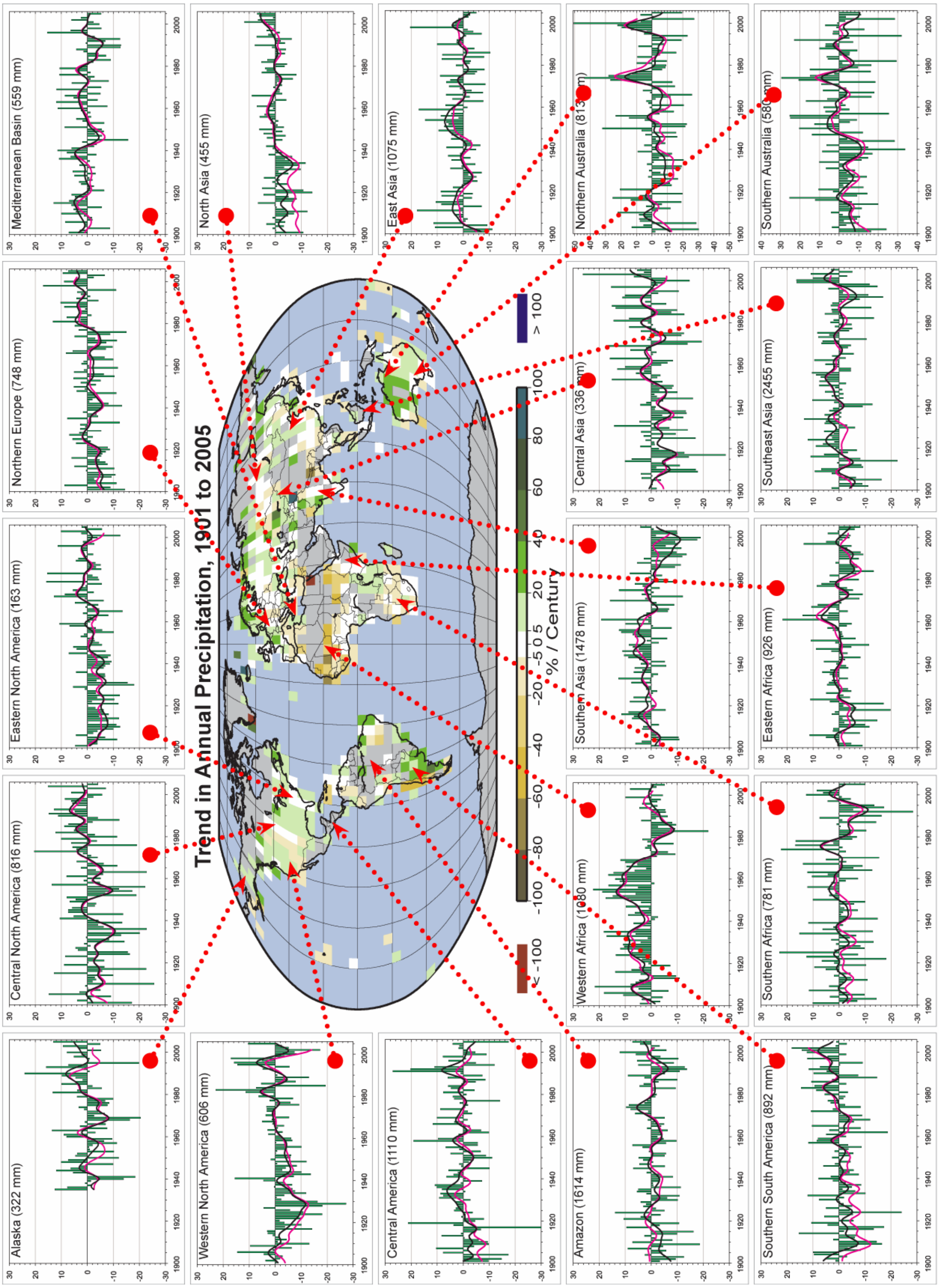
Trend in Annual Precipitation, 1901 to 2005
% / Century
< -100
-100
-80
-60
-40
-20
-5 0 5
20
40
60
80
100
> 100
Mediterranean Basin (559 mm)
North Asia (455 mm)
East Asia (1075 mm)
Northern Australia (813 mm)
Southern Australia (580 mm)
Northern Europe (748 mm)
Central Asia (336 mm)
Southeast Asia (2455 mm)
Eastern North America (163 mm)
Southern Asia (1478 mm)
Eastern Africa (926 mm)
Central North America (816 mm)
Western Africa (1080 mm)
Southern Africa (781 mm)
Alaska (322 mm)
Western North America (606 mm)
Central America (1110 mm)
Amazon (1614 mm)
Southern South America (892 mm)

Figure 3.14. Precipitation for 1900 to 2005. The central map shows the annual mean trends in % century^{-1}. Areas in grey have insufficient data to produce reliable trends. The surrounding time series of annual precipitation displayed (% of mean, with the mean given at top for 1961 to 1990) are for the named regions as indicated by the red arrows. The GHCN precipitation from NCDC was used for the annual green bars and the black decadal curves, and for comparison the CRU decadal curves are given in magenta. The range is +30% to –30% except for the two Australian panels. The regions are a subset of those defined in Table 11.1 (Chapter 11, Section 11.1) and include: Central North America, Western North America, Alaska, Central America, Eastern North America, Mediterranean basin, Northern Europe, North Asia, East Asia, Central Asia, Southeast Asia, Southern Asia, Northern Australia, Southern Australia, Eastern Africa, Western Africa, Southern Africa, Southern South America, and Amazon.

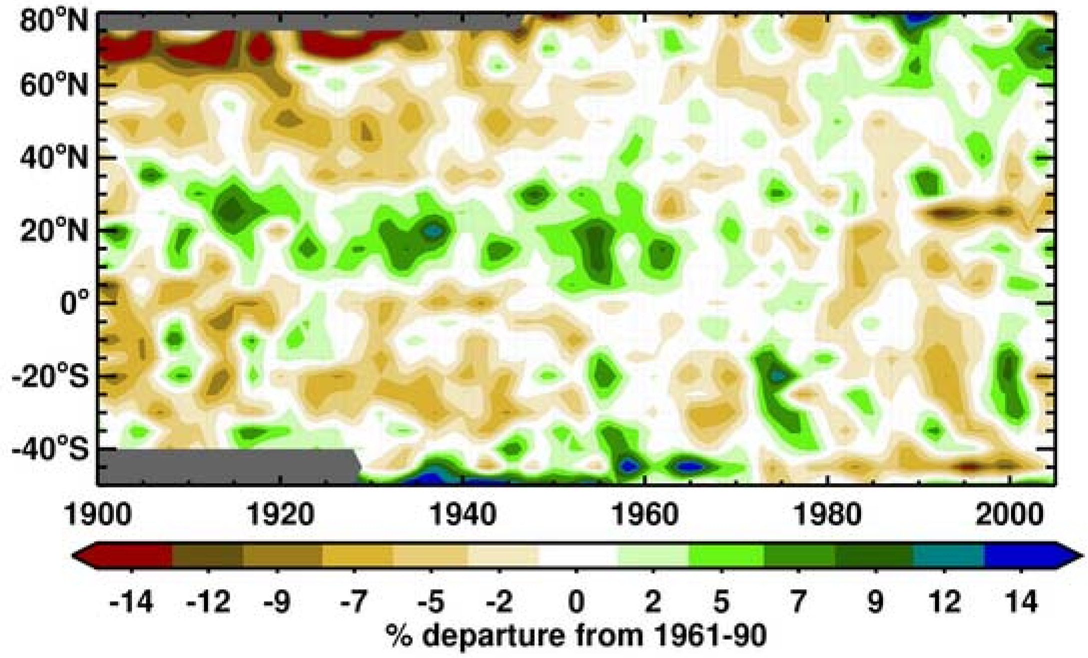

Figure 3.15. Latitude-time section of zonal average annual anomalies for precipitation (%) over land from 1900 to 2005, relative to their 1961 to 1990 means. The values are smoothed with a 1/12(1–3–4–3–1) filter to remove fluctuations less than about 6 years (see Appendix 3.A). The colour scale is nonlinear and grey areas indicate missing data.

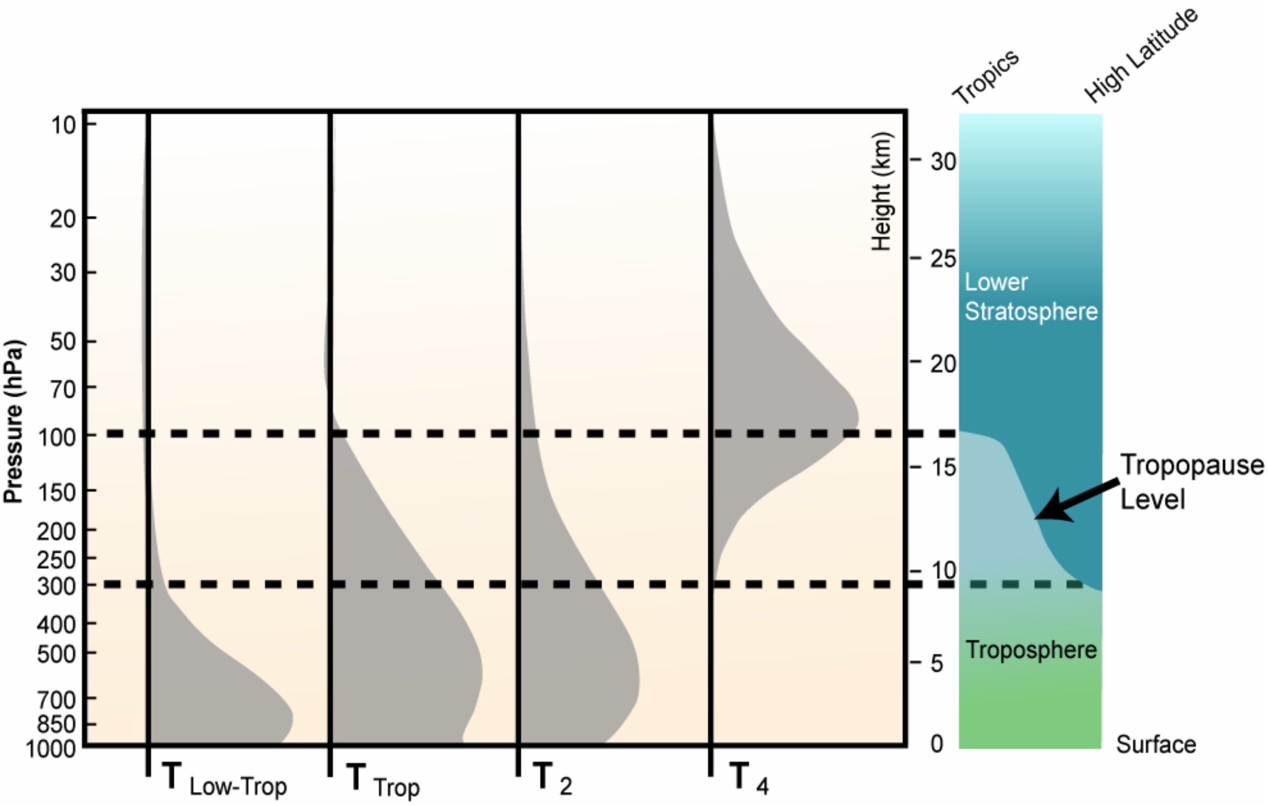

Figure 3.16. Vertical weighting functions depicting the layers sampled by satellite MSU measurements and their derivatives, and used also for radiosonde and reanalysis records. The right panel schematically depicts the variation in the tropopause from the tropics (left) to the high latitudes (right) and thus the dividing line between the stratosphere and troposphere. The fourth panel depicts T4 in the lower stratosphere, the third panel shows T2, the second panel shows the troposphere as a combination of T2 and T4 (Fu et al., 2004a), and the first panel shows $T2_{LT}$ from UAH for the low troposphere. Adapted from Karl et al. (2006).

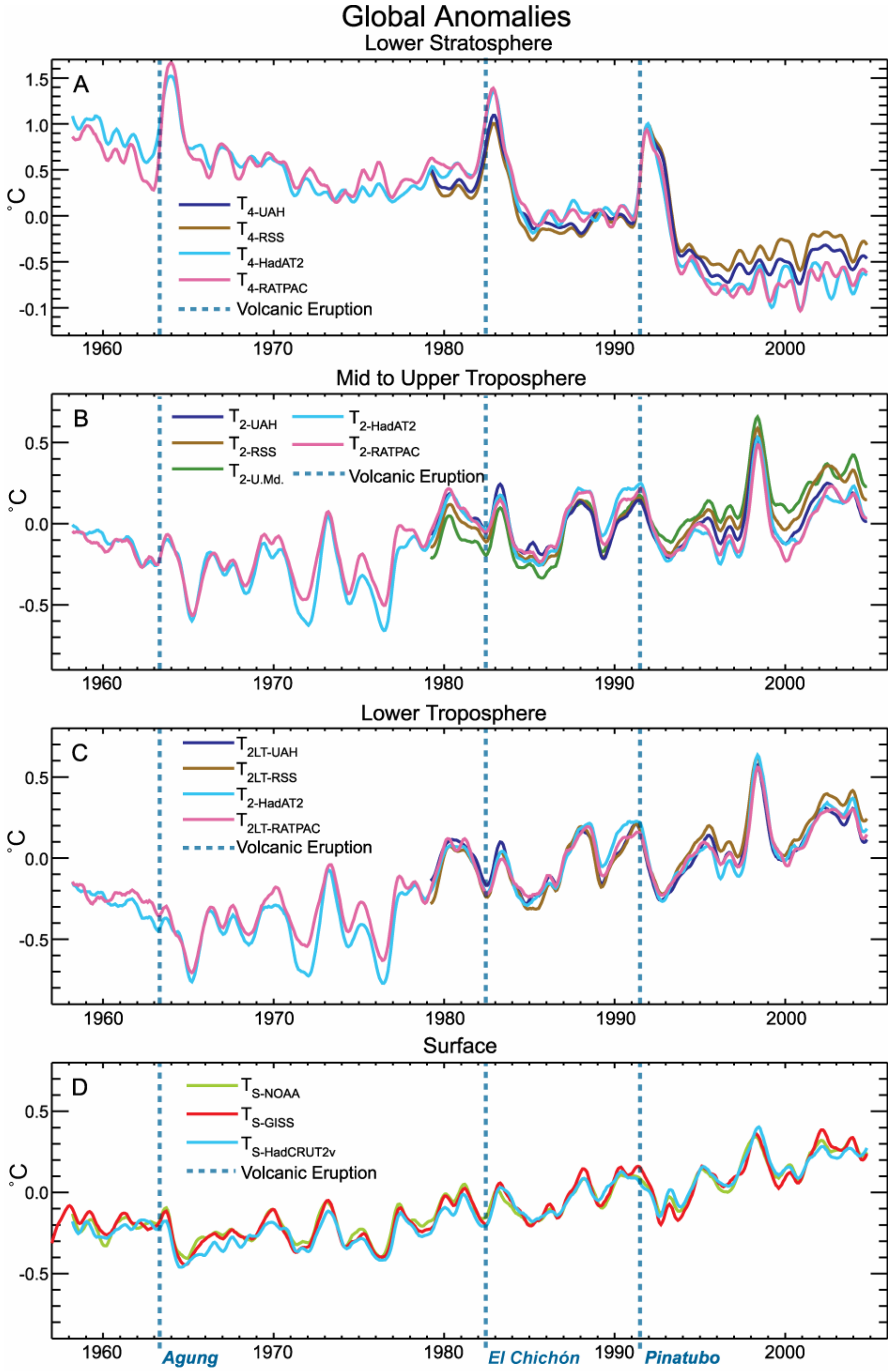

Figure 3.17. Observed surface and upper air temperature anomalies (°C). (A) Lower stratospheric T4, (B) Tropospheric T2, (C) Lower tropospheric $T2_{LT}$, from UAH, RSS, and VG2 (UMd; where available) MSU satellite analyses, UKMO HadAT2 and NOAA RATPAC radiosonde observations; (D): surface records from NOAA, NASA GISS and UKMO/CRU (HadCRUT2v). All time series are monthly mean anomalies relative to 1979 to 1997 smoothed with a 7 month running mean filter. Times of major volcanic eruptions are indicated by vertical blue dashed lines. From Karl et al. (2006).

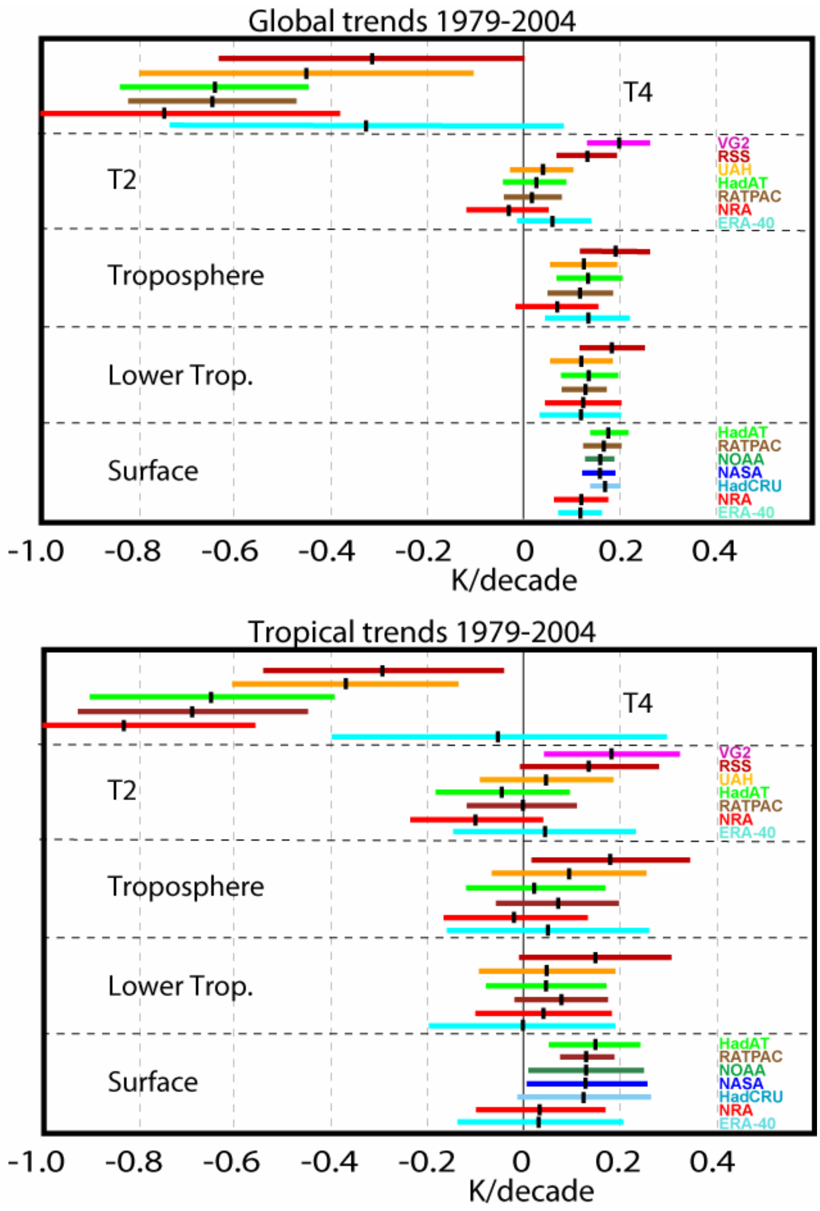

Figure 3.18. Linear trends of temperature (°C decade^{-1}) for 1979 to 2004 for the globe (top) and tropics 20°N–20°S (lower) for the MSU channels T4 (top panel) and T2 (second panel) or equivalent for radiosondes and reanalyses; for the troposphere (third panel) based on T2 with T4 used to statistically remove stratospheric influences (Fu et al., 2004a); the lower troposphere (fourth panel) based on the UAH retrieval profile; and the surface (bottom panel). Surface records are from NOAA/NCDC (green), NASA/GISS (blue) and HadCRUT2v (light blue). Satellite records are from UAH (orange), RSS (dark red) and VG2 (magenta); radiosonde based records are from NOAA RATPAC (brown), and HadAT2 (light green); and atmospheric reanalyses are from NRA (red), and ERA-40 (cyan). Confidence limits are 5 to 95% temporal sampling with an allowance for autocorrelation. Where the confidence limits exceed –1, the values are truncated. ERA-40 trends are only for 1979 to August 2002. Data from Karl et al. (2006; from D. Seidel courtesy J. Lanzante, and J. Christy).

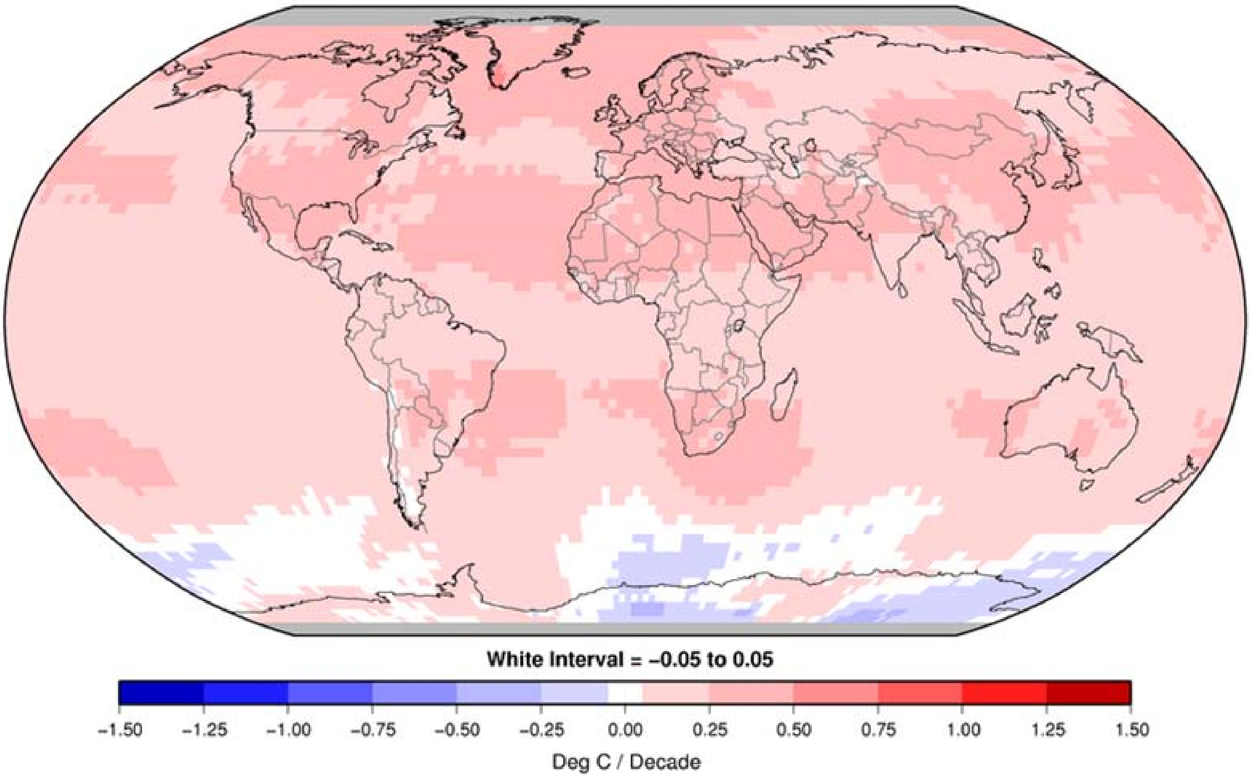

Figure 3.19. Linear trends of temperature (°C decade^{-1}) for 1979 to 2005 for the troposphere from RSS (based on T2 and T4 adjusted as in Fu et al., 2004a). Courtesy Q. Fu.

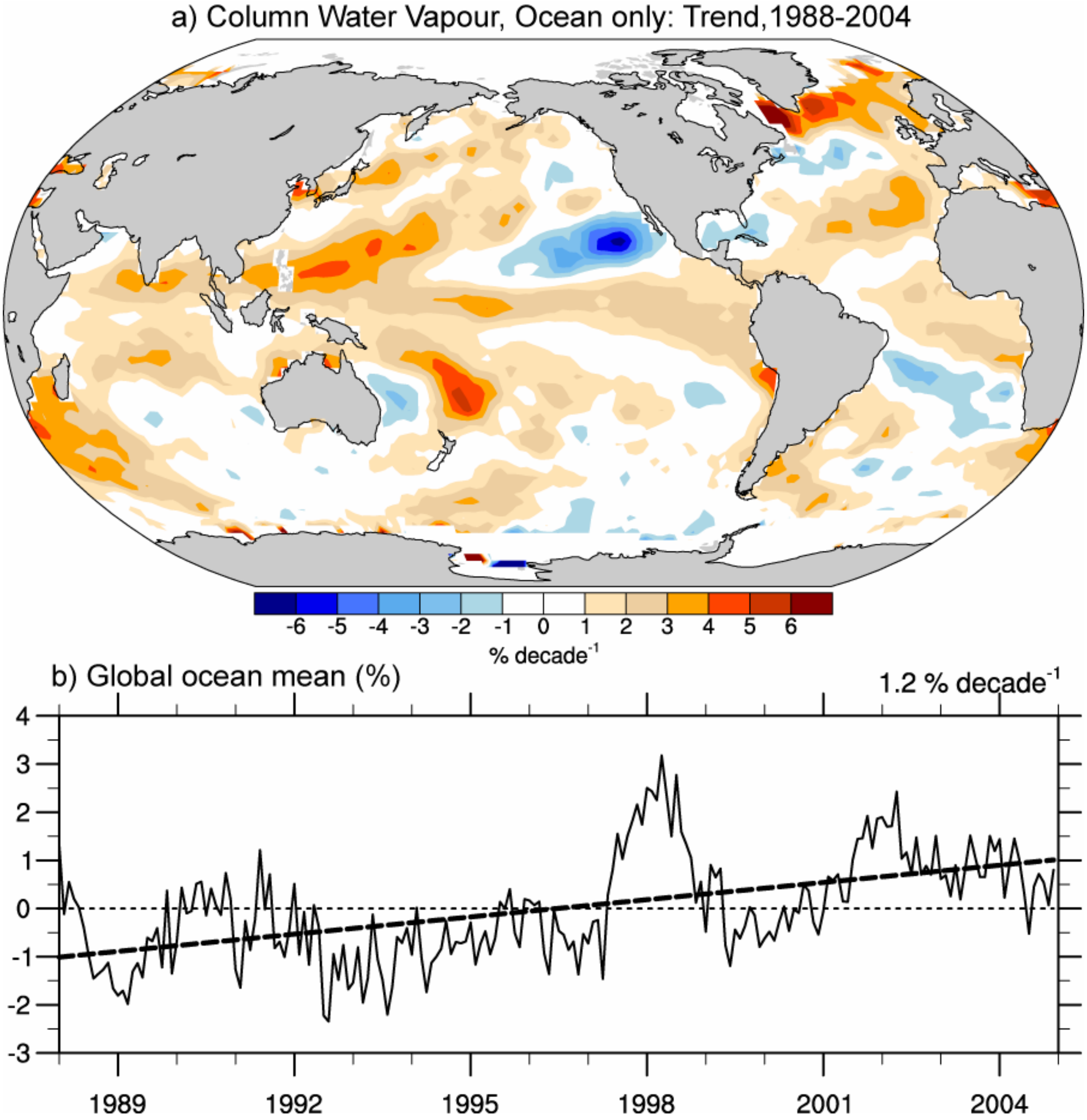

Figure 3.20. Linear trends in precipitable water (total column water vapour) for 1988 to 2004 in % decade^{-1} (top) and monthly time series of anomalies over the global ocean plus linear trend (bottom), from RSS SSM/I (updated from Trenberth et al., 2005a).

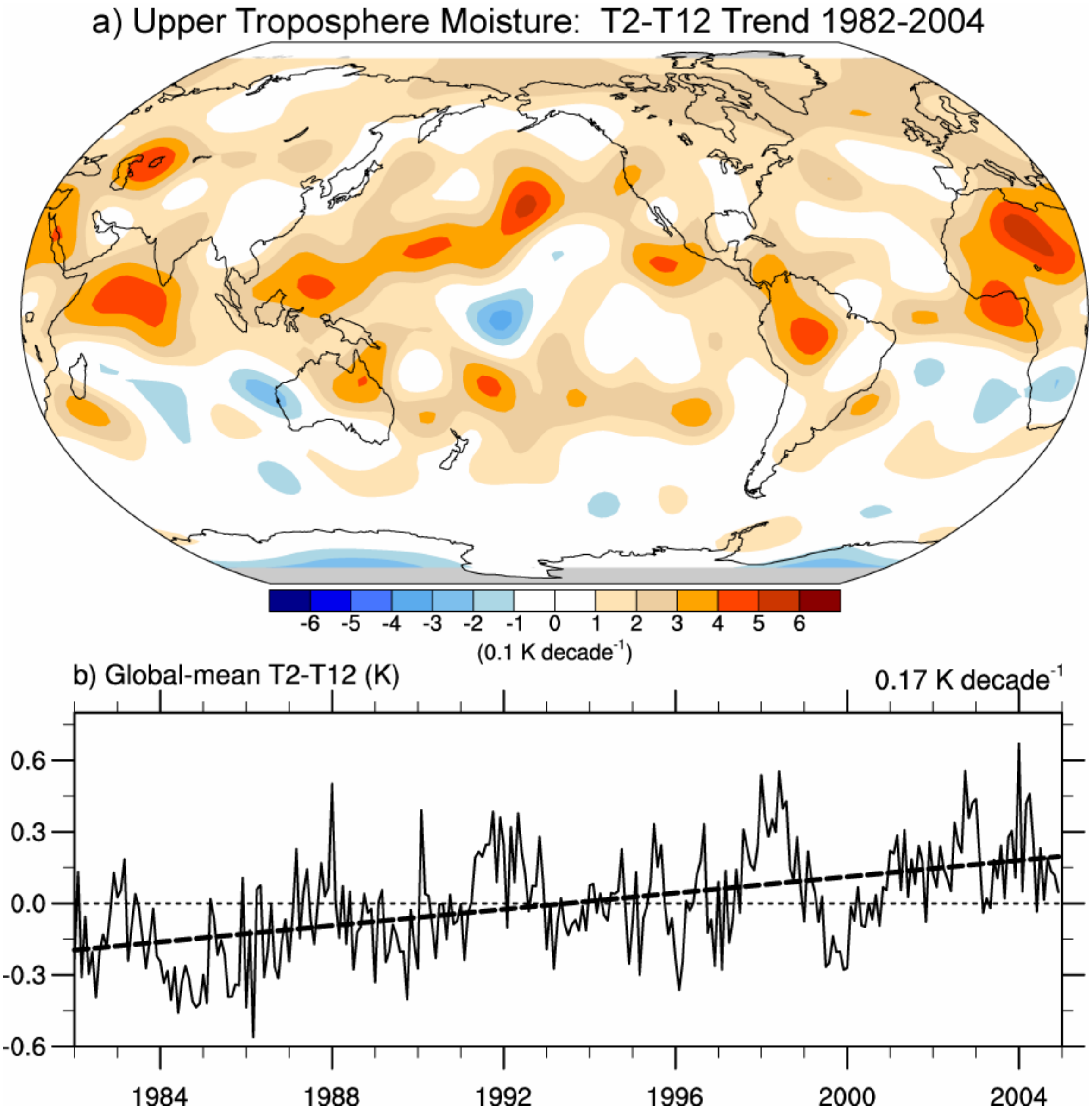

Figure 3.21. The radiative signature of upper tropospheric moistening is given by upward linear trends in T2–T12 for 1982 to 2004 in 0.1 K decade^{-1} (top) and monthly time series of the global-mean (80°N to 80°S) anomalies and linear trend (dashed) (bottom). Data are from the RSS T2 and HIRS T12 (Soden et al., 2005). The map is smoothed to T31 resolution.

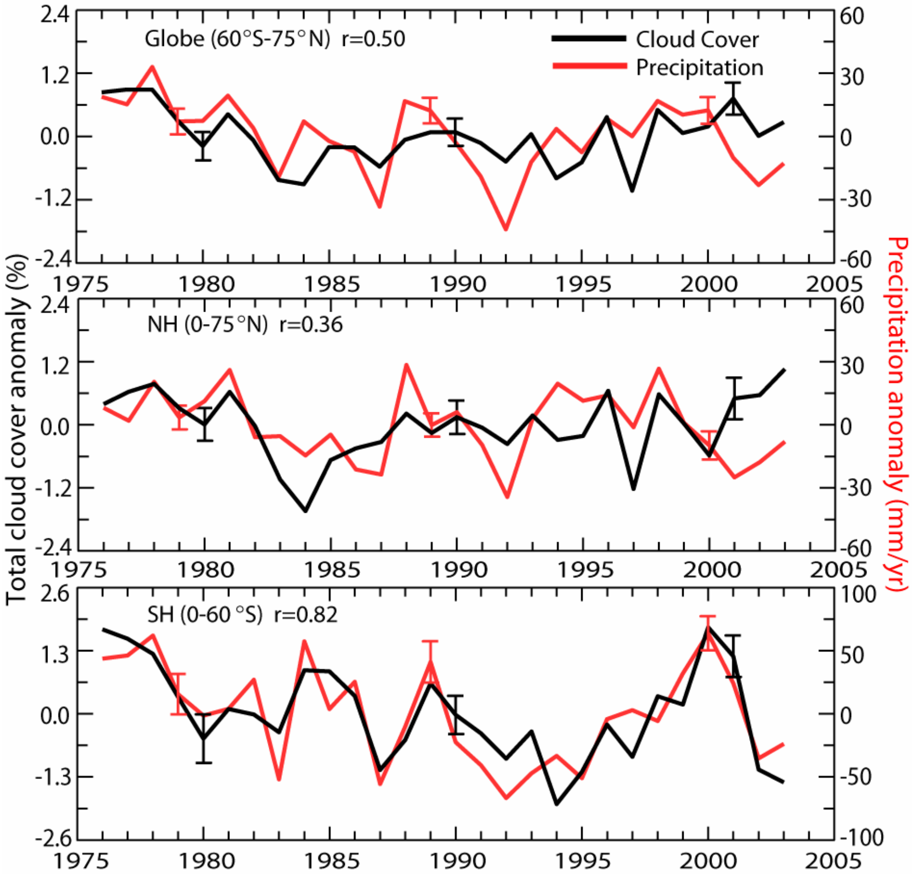

Figure 3.22. Annual total land (excluding the U.S. and Canada) cloud cover (black) and precipitation (red) anomalies from 1976 to 2003 over global (60°S–75°N), NH and SH regions, with the correlation coefficient (r) shown at the top. The cloud cover is derived by gridding and area-averaging synoptic observations and the precipitation is from Chen et al. (2002). Typical 5 to 95% error bars for each decade are estimates using inter-grid-box variations (from Dai et al., 2006).

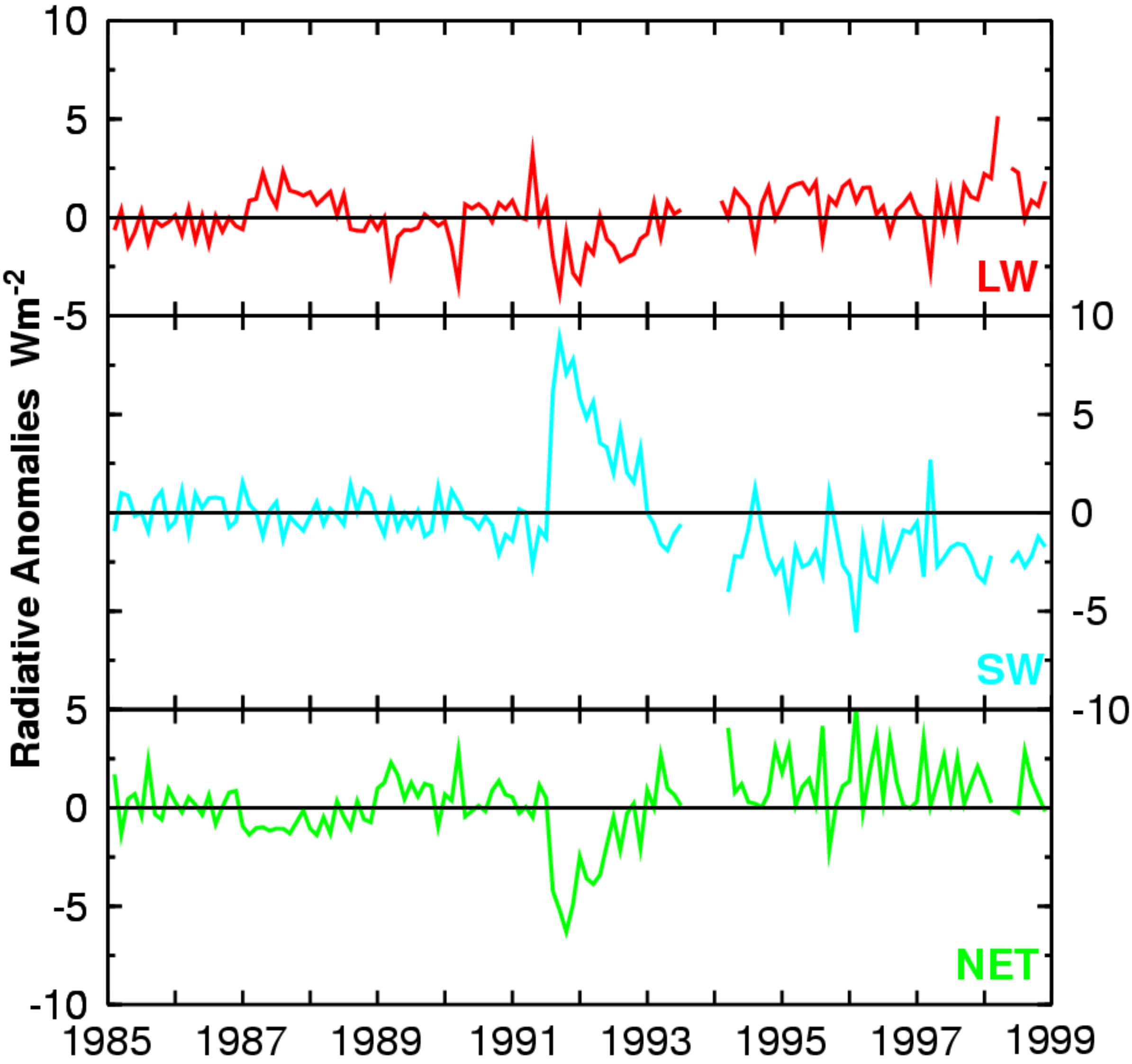

Figure 3.23. Tropical mean (20°S to 20°N) TOA flux anomalies for LW, SW, and NET radiative fluxes from 1985 to 1999 [NET = –(LW+SW)]. Coloured lines are observations from ERBS Edition 3_Rev1 data from Wong et al. (2006), updated from Wielicki et al. (2002a) including spacecraft altitude and SW dome transmission corrections.

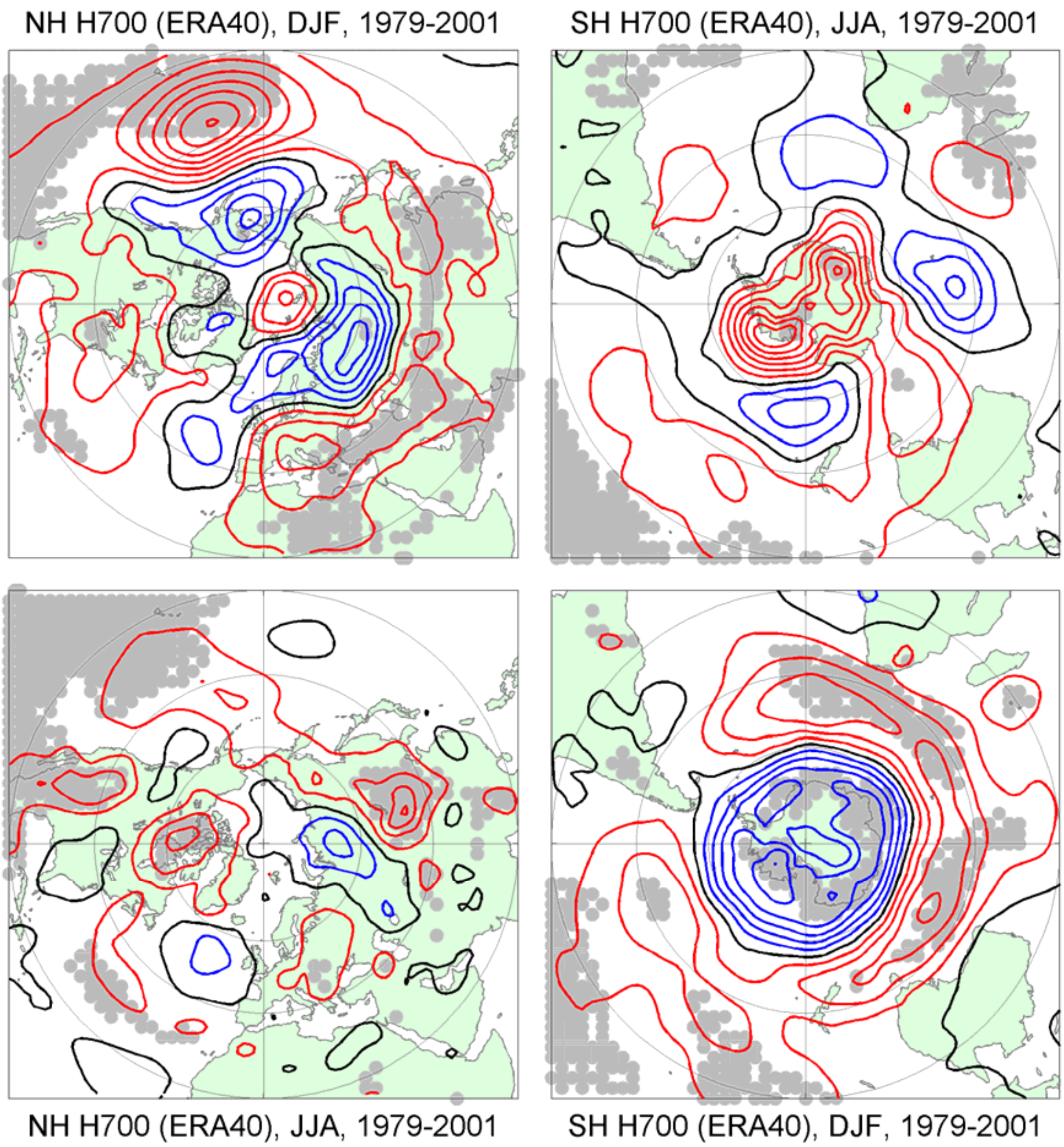

Figure 3.24. Linear trends in ERA-40 700 hPa geopotential height, 1979 to 2001 for DJF (top left and bottom right) and JJA (bottom left and top right), for the NH (left) and SH (right). Trends are contoured in 5 gpm decade^{-1} and are calculated from seasonal means of daily 1200 UTC fields. Red contours are positive, blue negative, and black zero; the grey background indicates 1% statistical significance using a standard least-squares F-test and assuming independence between years.

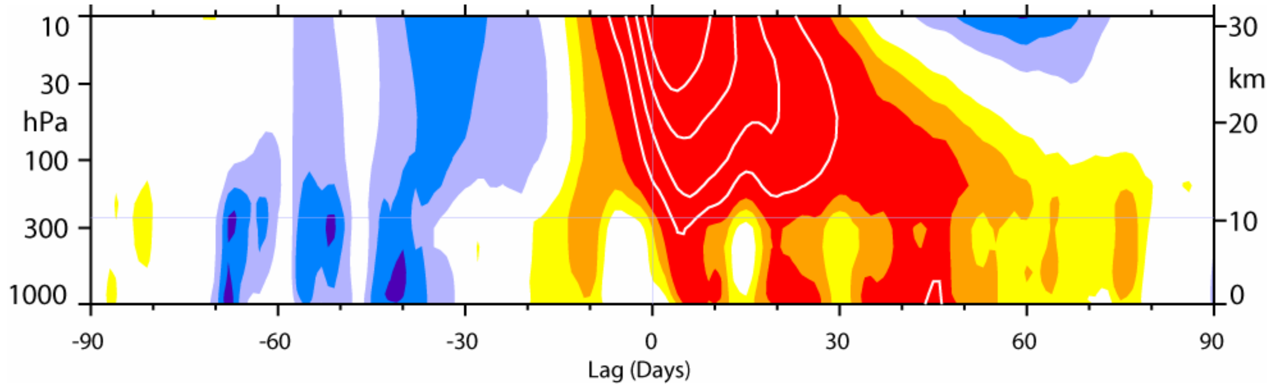

Box 3.3, Figure 1. Composites of time-height development of the NAM index for 18 weak vortex events. The events are selected by the dates on which the 10 hPa annular mode index crossed –3.0. Day 0 is the start of the weak vortex event. The indices are nondimensional; the contour interval for the colour shading is 0.25, and 0.5 for the white lines. Values between –0.25 and 0.25 are not shaded. Yellow and red shading indicates negative NAM indices and blue shading indicates positive indices. The thin horizontal lines indicate the approximate boundary between the troposphere and the stratosphere. Modified from Baldwin and Dunkerton (2001).

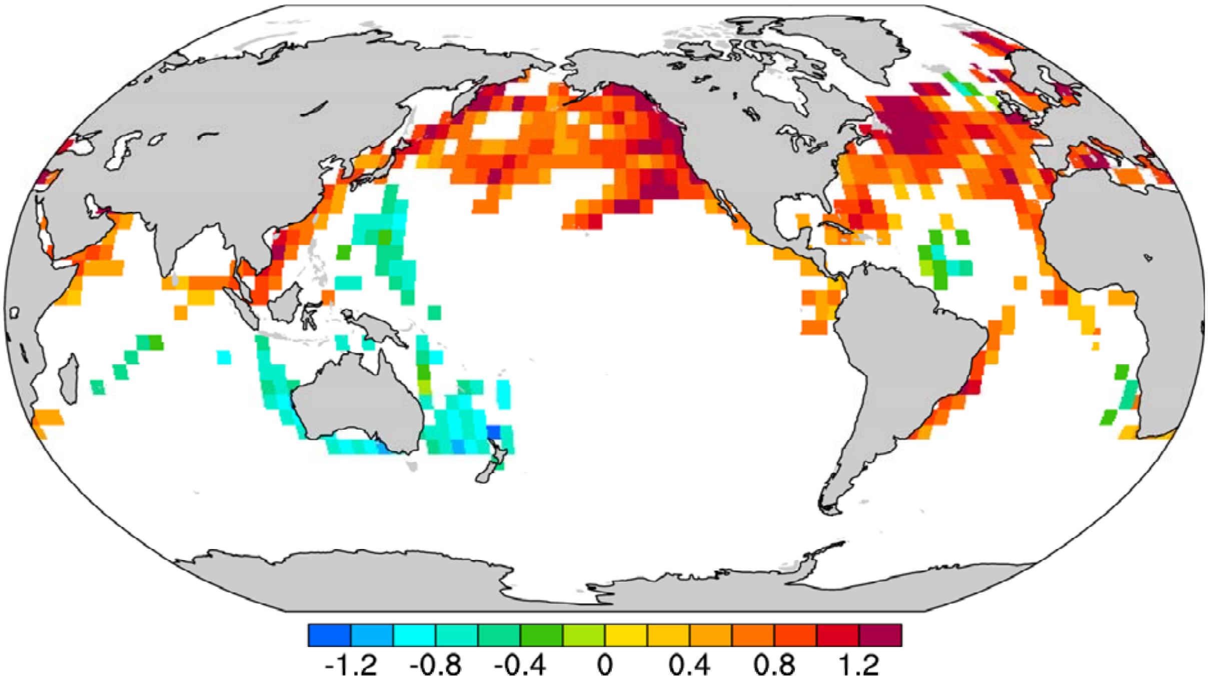

Figure 3.25. Estimates of linear trends in significant wave height (cm decade^{-1}) for the regions along the major ship routes for the global ocean for 1950 to 2002. Trends are shown only for the locations where they are significant at the 5% level. Adapted from Gulev and Grigorieva (2004).

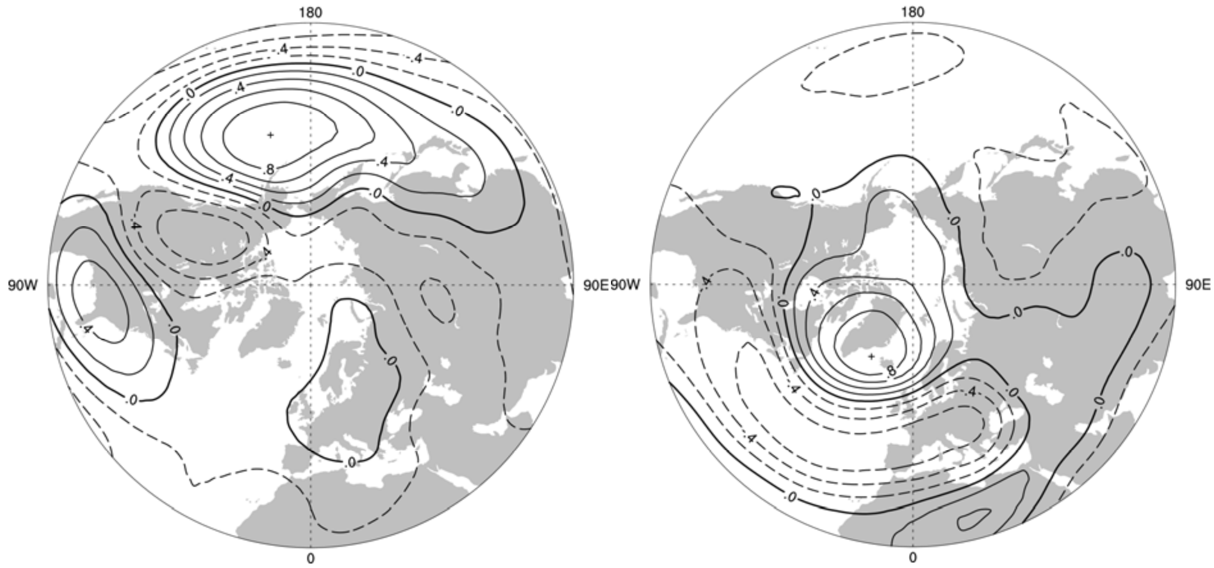

Figure 3.26. The PNA (left) and NAO (right) teleconnection patterns, shown as one-point correlation maps of 500 hPa geopotential heights for boreal winter (DJF) over 1958 to 2005. In the left panel, the reference point is 45°N, 165°W, corresponding to the primary centre of action of the PNA pattern, given by the + sign. In the right panel, the NAO pattern is illustrated based on a reference point of 65°N, 30°W. Negative correlation coefficients are dashed, and the contour increment is 0.2. Adapted from Hurrell et al. (2003).

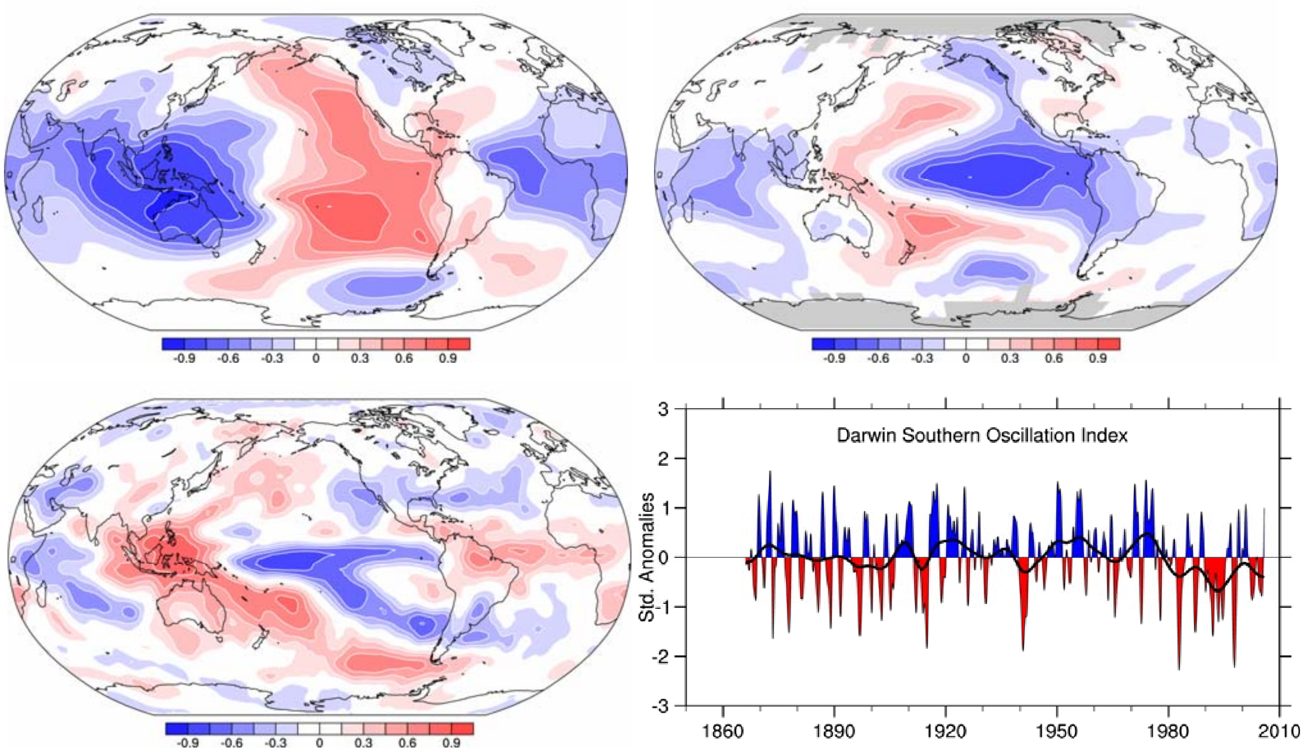

Figure 3.27. Correlations with the SO index (SOI), based on normalised Tahiti minus Darwin sea level pressures, for annual (May to April) means for sea level pressure (top left) and surface temperature (top right) for 1958 to 2004, and GPCP precipitation for 1979 to 2003 (bottom left) updated from Trenberth and Caron (2000). The Darwin-based SOI from 1866 to 2005 (Können et al., 1998; lower right) features monthly values with an 11-point low pass filter, which effectively removes fluctuations with periods of less than 8 months (Trenberth, 1984). The thick black line represents the decadal filter (Appendix 3.A). Red values indicate positive sea level pressure anomalies at Darwin and thus El Niño conditions.

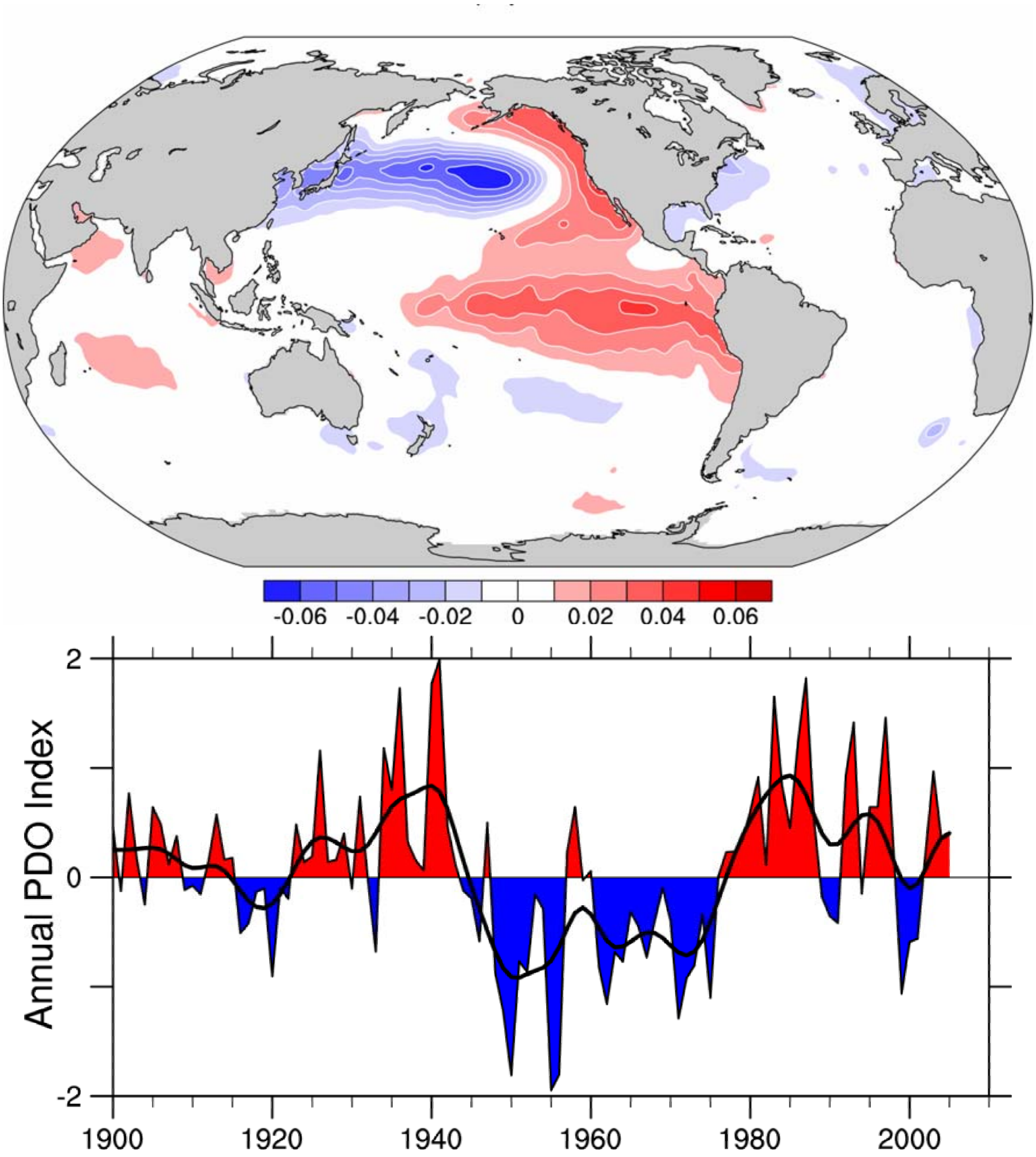

Figure 3.28. Pacific Decadal Oscillation. (top) SST based on the leading EOF SST pattern for the Pacific basin north of 20°N for 1901 to 2004 (updated; see Mantua et al., 1997; Power et al., 1999b) and projected for the global ocean (units are nondimensional); and (bottom) annual time series (updated from Mantua et al., 1997); the thick black curve uses the decadal filter (Appendix 3.A).

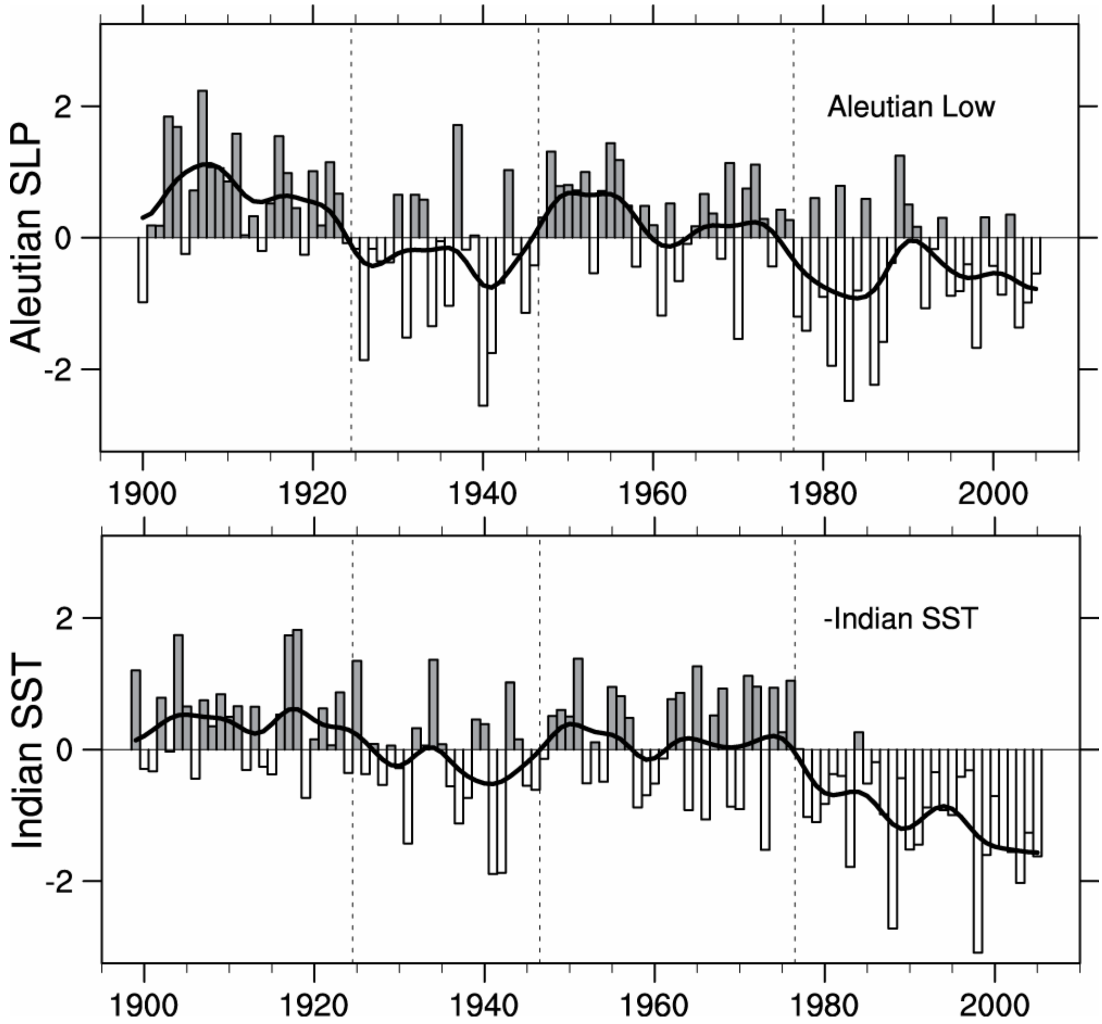

Figure 3.29. Top: Time series of the NPI (sea level pressure during December–March averaged over the North Pacific 30–65°N, 160°E–140°W) from 1900 to 2005 expressed as normalized departures from the long-term mean (each tick mark on the ordinate represents two standard deviations, or 5.5 hPa). This record reflects the strength of the wintertime Aleutian Low Pressure System, with positive (negative) values indicative of a weak (deep) Aleutian Low. The bars give the wintertime series and the thick curve is the decadal low-pass filter (Appendix 3.A). Values were updated and extended to earlier decades from Trenberth and Hurrell (1994). Lower: As above but for SSTs averaged over the Tropical Indian Ocean (10°S–20°N, 50–125°E; (each tick mark represents two standard deviations, 0.36°C). This record has been inverted to facilitate comparison with the top panel. The dashed vertical lines mark years of transition in the Aleutian Low record (1925, 1947, 1977). Updated from Deser et al. (2004).

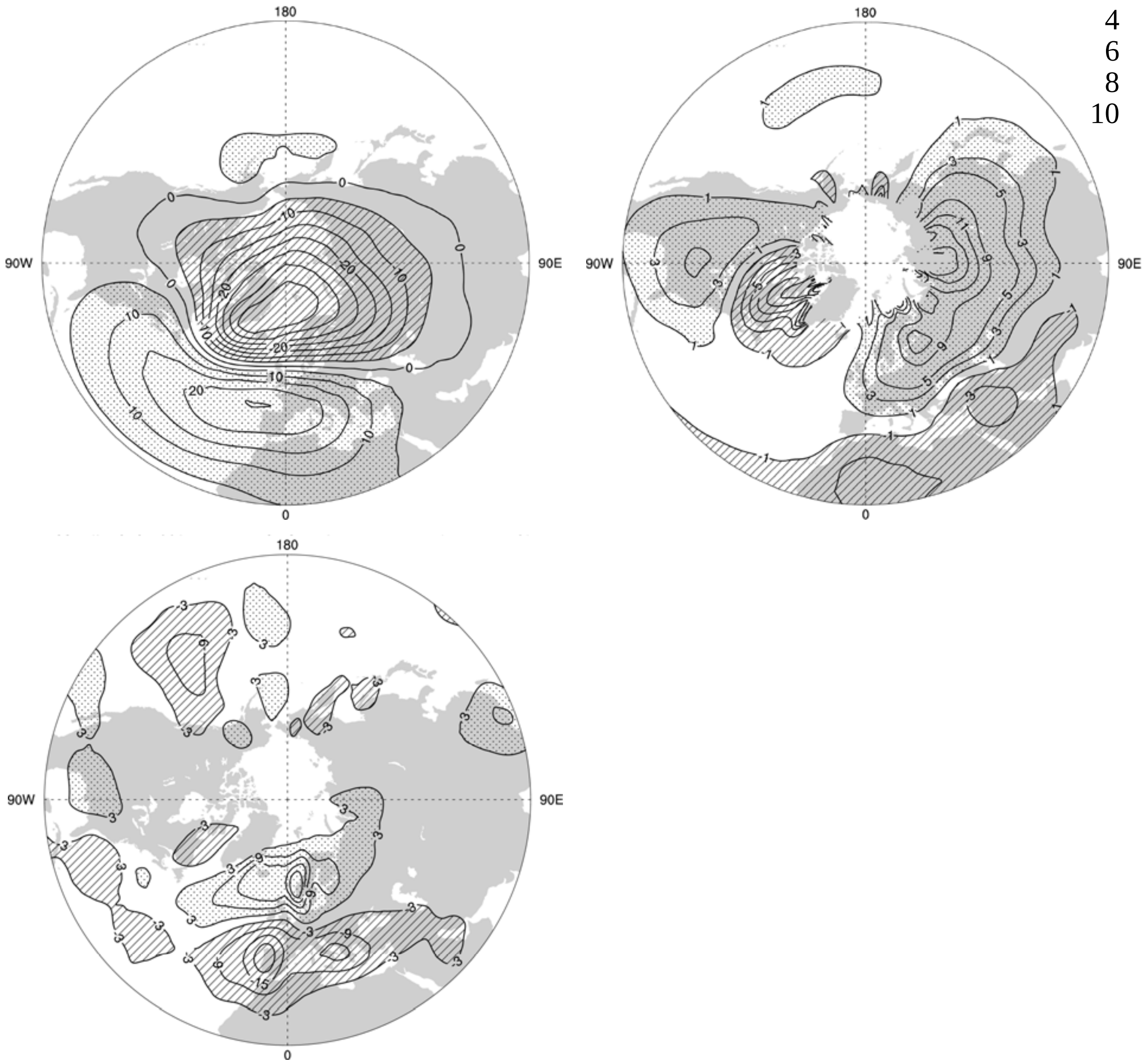

Figure 3.30. Changes in winter (December–March) corresponding to a unit deviation of the NAO index over 1900 to 2005 for (top left) mean sea level pressure in ($\times 10^{-1}$ hPa). Values greater than 0.5 hPa are stippled and <–0.5 hPa are hatched. (Top right) land surface air and sea surface temperatures ($\times 10^{-1}$°C). The contour increment is 0.2°C. Temperature changes >0.1°C are indicated by stippling, and those <–0.1°C are indicated by hatching. Regions of insufficient data (e.g., over much of the Arctic) are not contoured. (Bottom left) precipitation for 1979 to 2003 based on GPCP ($\times 10^{-1}$ mm/day). Stippling indicates values >0.3 mm/day and hatching values less than –0.3 mm/day. Contour interval 0.6 mm/day. Adapted and updated from Hurrell et al. (2003).

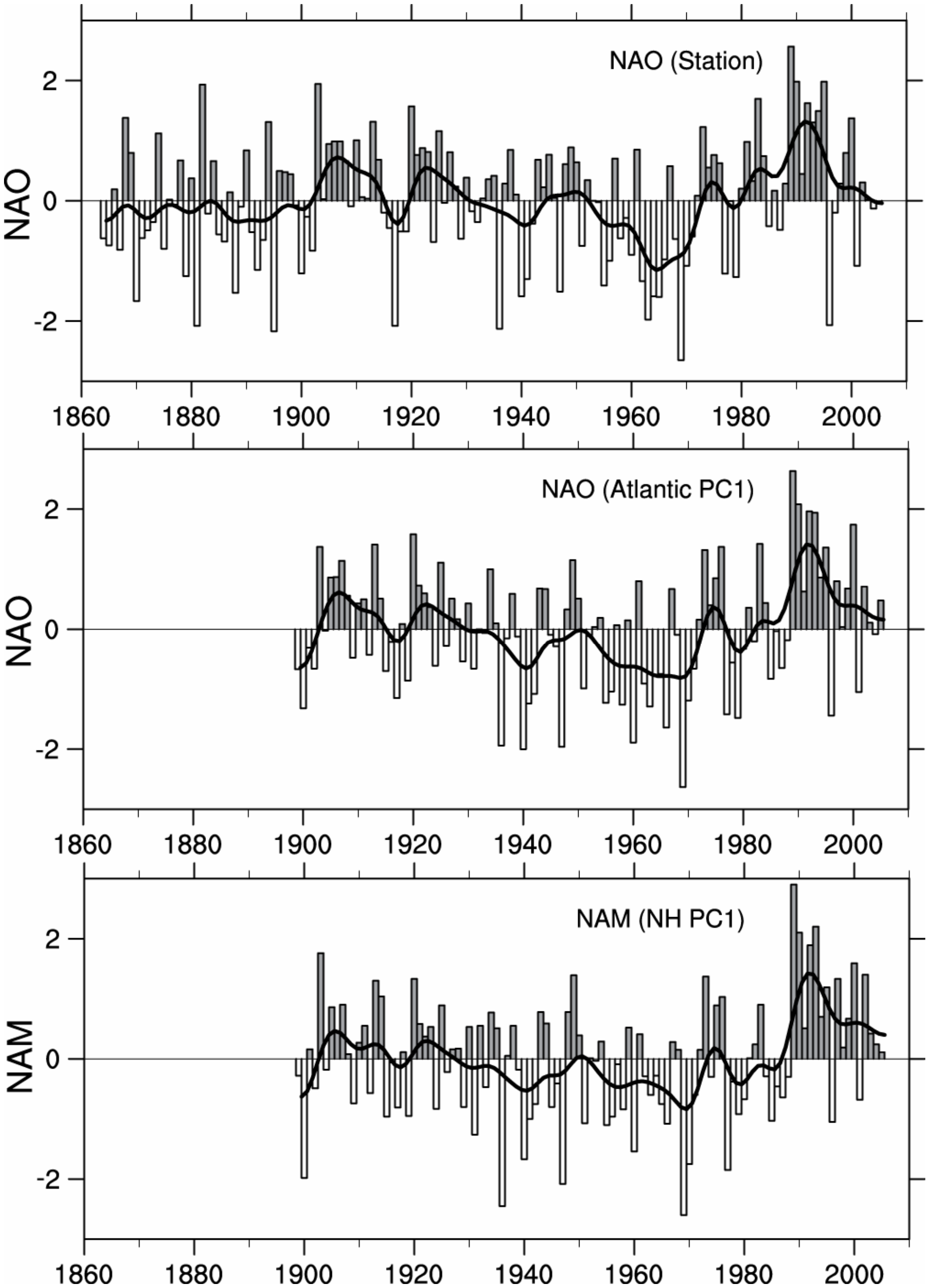

Figure 3.31. Normalized indices of the mean winter (December–March) NAO developed from sea level pressure data. In the top panel, the index is based on the difference of normalized sea level pressure between Lisbon, Portugal and Stykkisholmur/Reykjavik, Iceland from 1864 to 2005. The average winter sea level pressure data at each station were normalized by division of each seasonal pressure anomaly by the long-term (1864 to 1983) standard deviation. In the middle panel, the index is the principal component time series of the leading empirical orthogonal function (EOF) of Atlantic-sector sea level pressure. In the lower panel, the index is the principal component time series of the leading EOF of NH sea level pressure. The heavy solid lines represents the decadal filter (Appendix 3.A). The individual bar corresponds to the January of the winter season (e.g., 1990 is the winter of 1989/1990). See http://www.cgd.ucar.edu/~jhurrell/nao.html for updated time series. Updated from Hurrell et al. (2003).

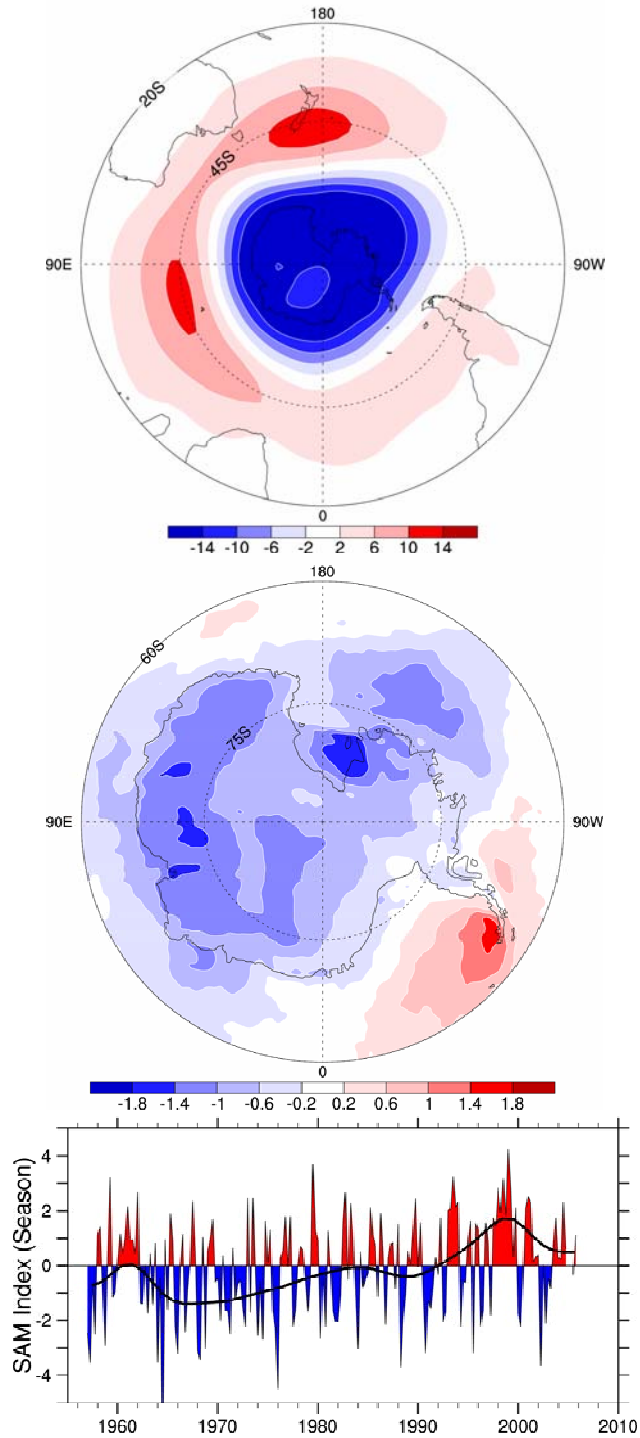

Figure 3.32. Bottom: Seasonal values of the SAM index calculated from station data (updated from Marshall, 2003). The thick black line is the decadal filter (Appendix 3.A). Top: SAM geopotential height pattern as a regression based on the SAM time series for seasonal anomalies at 850 hPa (see also Thompson and Wallace, 2000). Middle: the regression of changes in surface temperature (°C) over the 23-year period (1982–2004) corresponding to a unit change in the SAM index, plotted south of 60°S. Values exceeding about 0.4°C in magnitude are significant at the 1% significance level (adapted from Kwok and Comiso, 2002b).

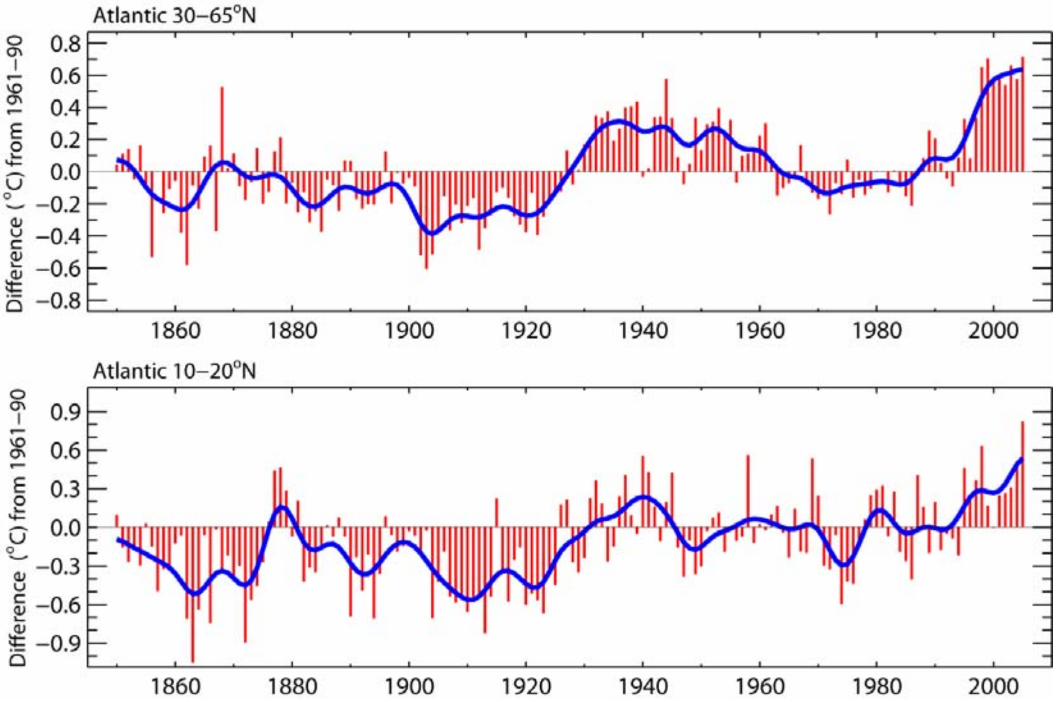

Figure 3.33. Atlantic Multidecadal Oscillation index 1850 to 2005 represented by annual anomalies of SST in the extratropical North Atlantic (30–65°N) (top), and in a more muted fashion in the tropical Atlantic (10–20°N) SST anomalies. Both series come from HadSST2 (Rayner et al., 2006) and are relative to 1961 to 90 mean (°C). The blue curve depicts the decadal filter (Appendix 3.A).

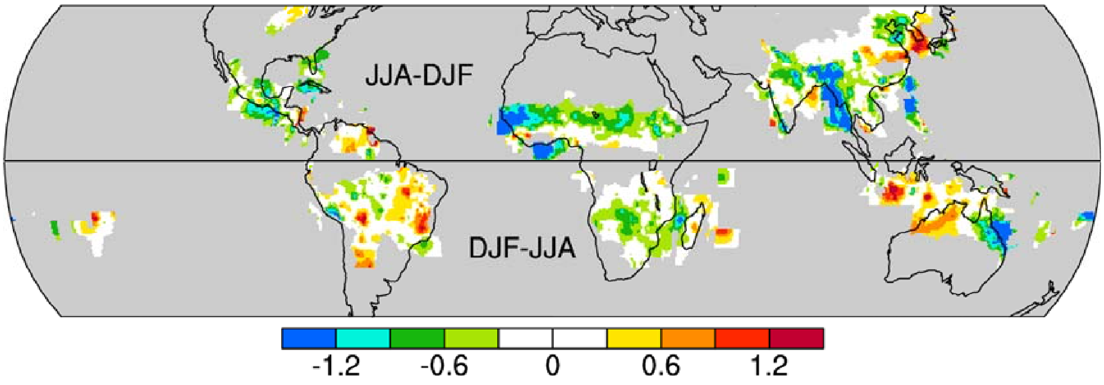

Figure 3.34. Change in the mean annual range of precipitation: 1976 to 2003 minus 1948 to 1975 periods in mm/day. Blue/green (red/yellow) colour denotes decreasing (increasing) annual range of the monsoon rainfall. Grey areas indicate missing values (oceans) or areas with insignificant annual changes. Data used are obtained from NCEP (PREC/L) (Data from Chen et al., 2002; see Wang and Ding, 2006).

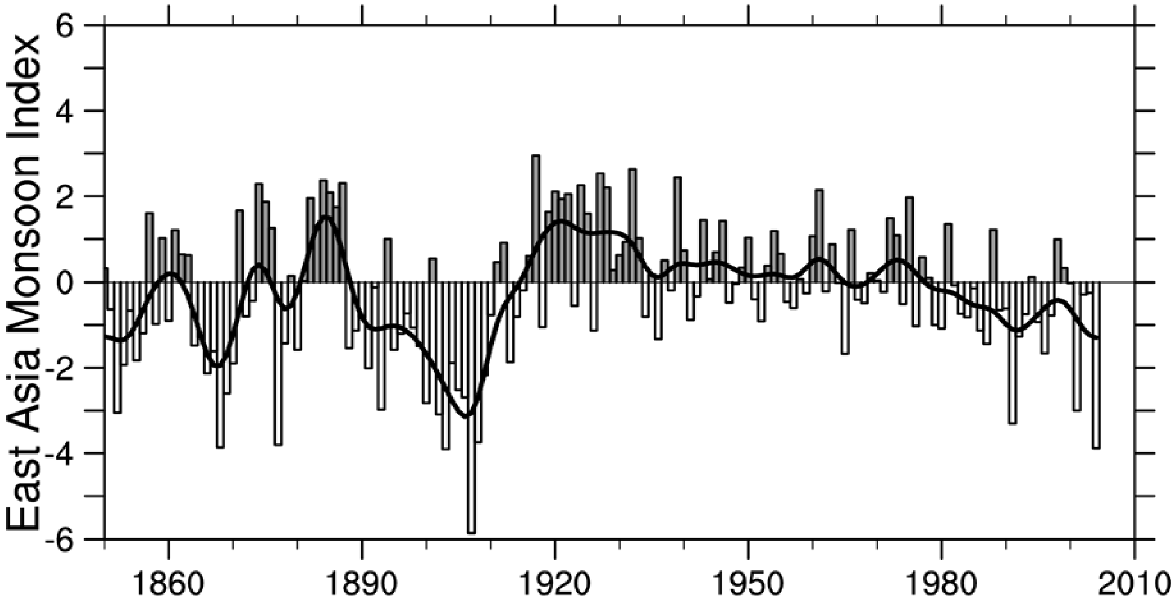

Figure 3.35. East Asia summer monsoon index derived from MSLP gradients between land and ocean in the east Asia region. The definition of the index is based on Guo et al. (2003) but was recalculated based on the HadSLP2 (Allan and Ansell, 2006) data set. Annual values are shown and the black smooth curve is the decadal filter (Appendix 3.A).

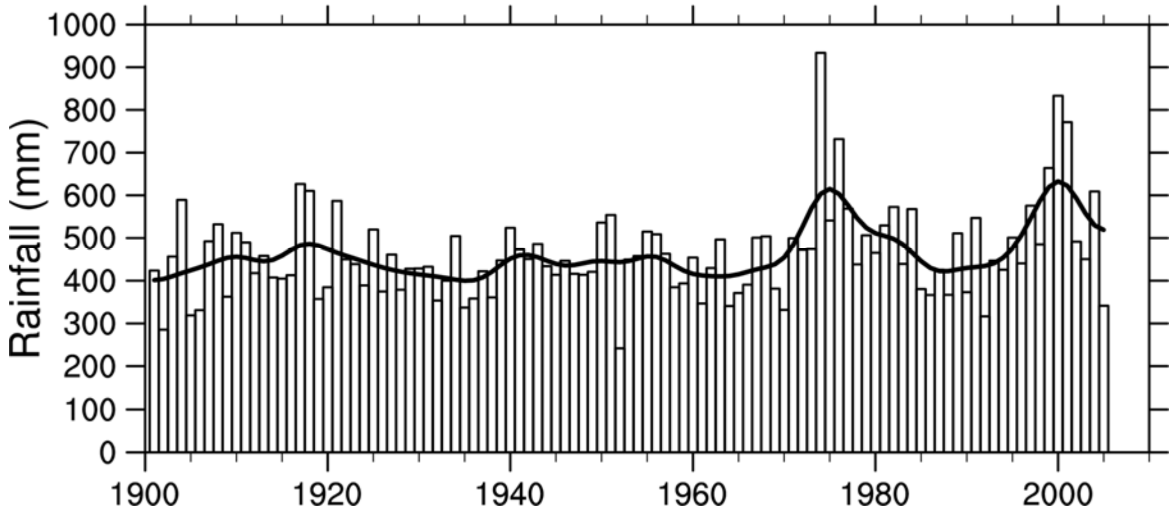

Figure 3.36. Time series of northern Australian (north of 26°S) wet-season (October–April) rainfall during 1900/1901 to 2004/2005. Individual years are plotted according to the date of the January. Black curve indicates the decadal filter (Appendix 3.A). Data from Australian Bureau of Meteorology.

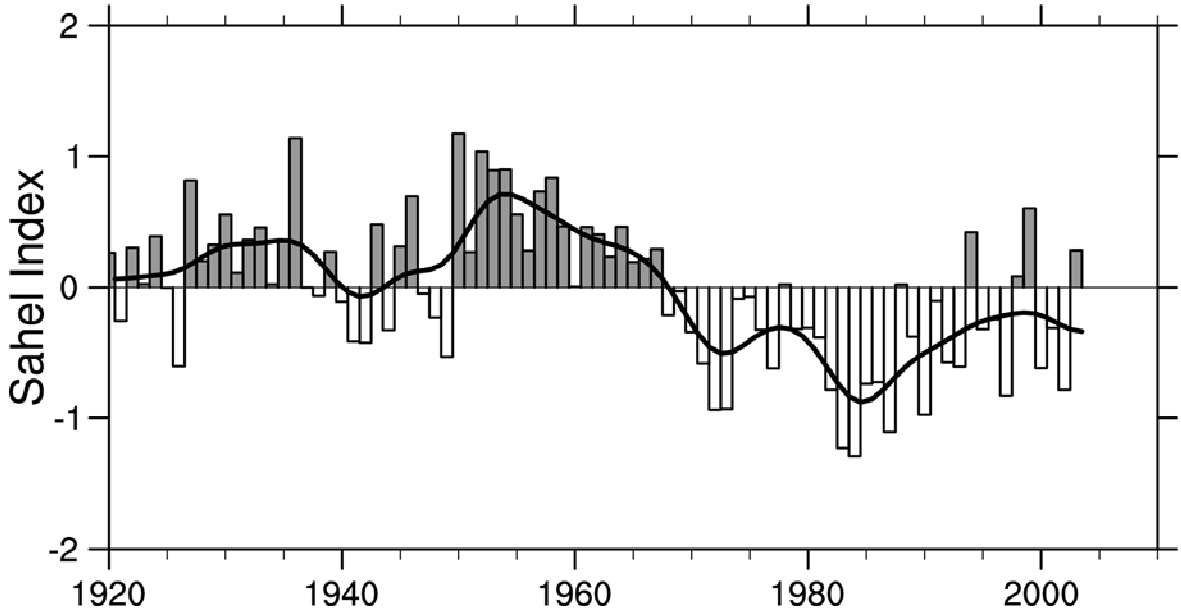

Figure 3.37. Time series of Sahel (10–20ºN, 18ºW–20ºE) regional rainfall for April to October from 1920 to 2003 derived from gridding normalized station anomalies and then averaging using area weighting (adapted from Dai et al., 2004a). The decadal filter is from Appendix 3.A.

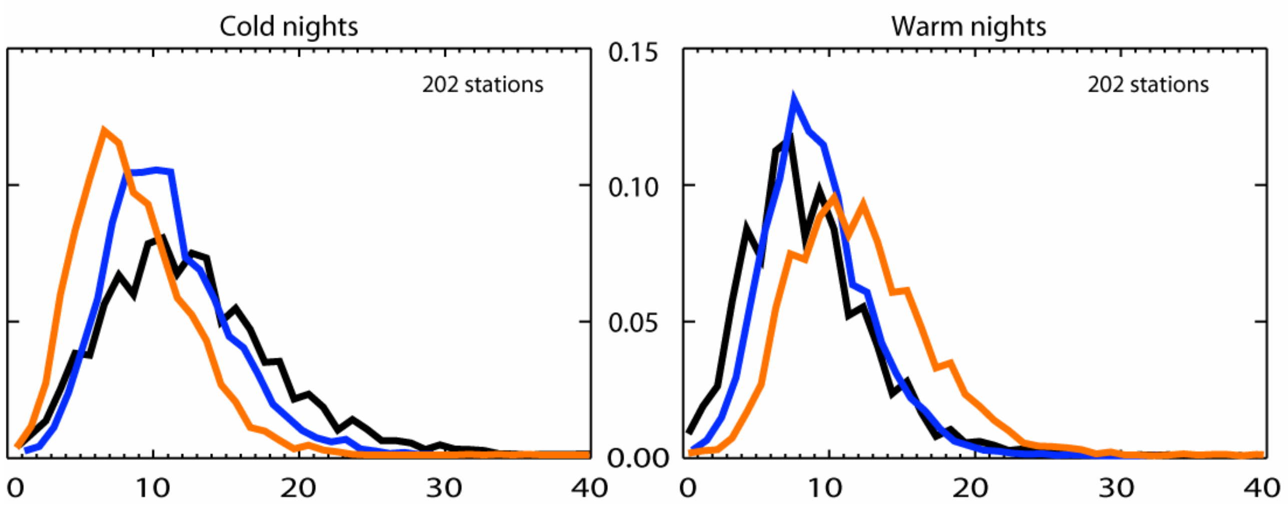

Figure 3.38. Annual probability distribution functions for temperature indices for 202 global stations with at least 80% complete data between 1901 and 2003 for 3 time periods: 1901 to 1950 (black), 1951 to 1978 (blue) and 1979 to 2003 (red). The x-axis represents the percentage of time during the year when the indicators were below the 10th percentile (left) for cold nights or above the 90th percentile (right) for warm nights. From Alexander et al. (2006).

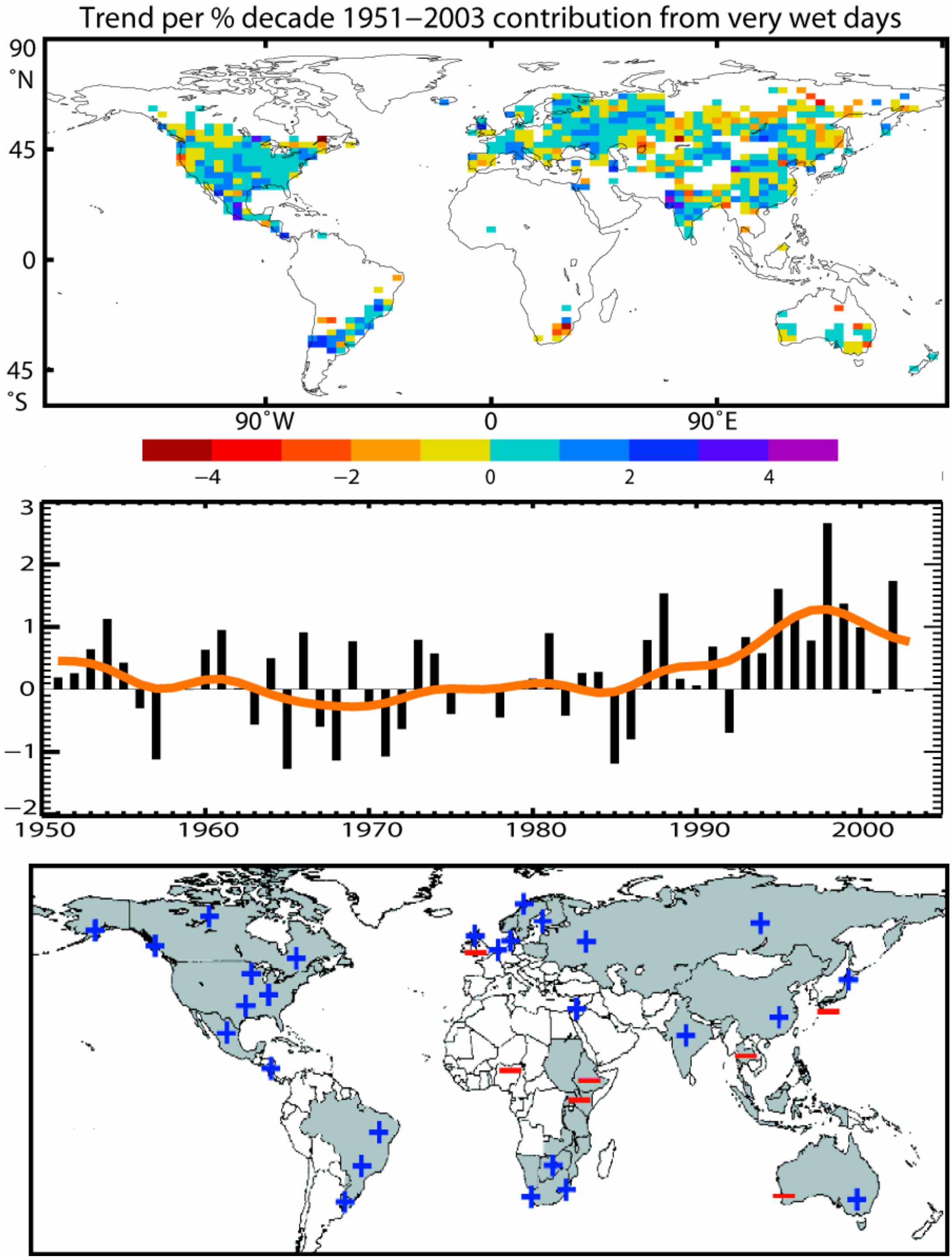

Figure 3.39. Upper: Observed trends (%) per decade for 1951 to 2003 for the contribution to total annual precipitation from very wet days corresponding to the 95th percentile. Trends were only calculated for grid boxes where both total and the 95th percentile had at least 40 years of data during this period and had data until at least 1999. Middle: Anomalies of the global annual time series (with respect to 1961 to 1990) defined as the percentage change of very wet day contribution from the base period average (22.5%). The red line shows decadal variations. From Alexander et al. (2006). Lower: Regions where disproportionate changes in heavy and very heavy precipitation during the past decades were documented compared to the change in the annual and/or seasonal precipitation (updated from Groisman et al., 2005). Thresholds used to define "heavy" and "very heavy" precipitation vary by season and region. However, changes in heavy precipitation frequencies are always greater than changes in precipitation totals and, in some regions, an increase in heavy and/or very heavy precipitation occurred while no change or even a decrease in precipitation totals was observed.

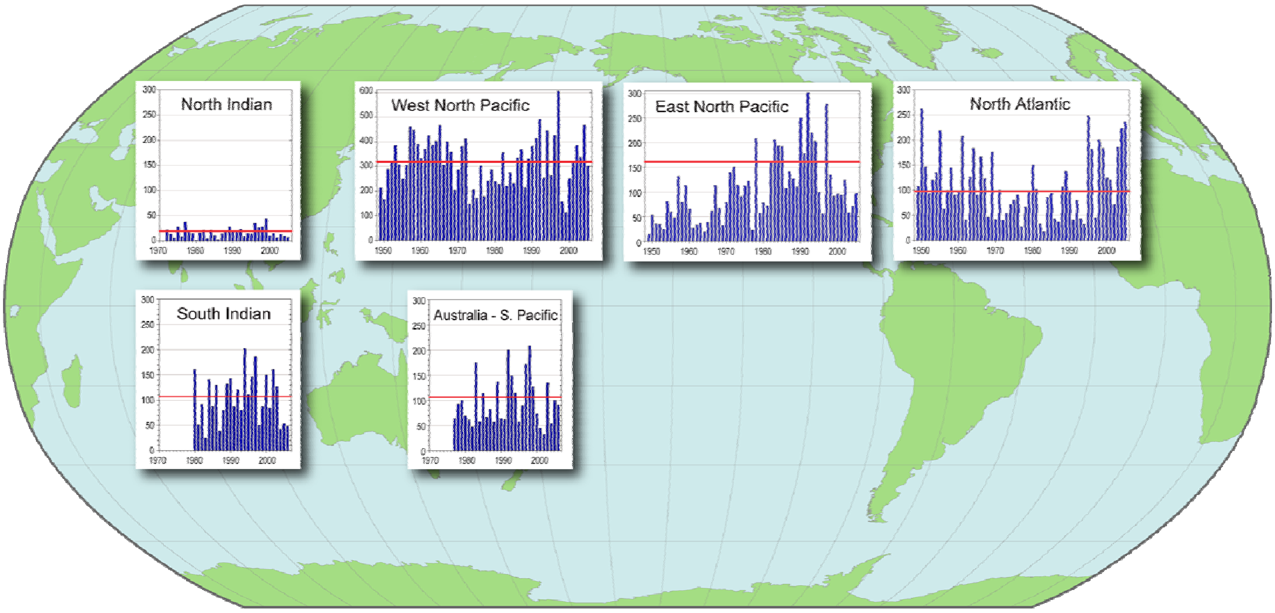

Figure 3.40. Seasonal values of the Accumulated Cyclone Energy (ACE) index for the North Indian, South Indian, West North Pacific, East North Pacific, North Atlantic and combined Australian-South Pacific regions. The vertical scale in the West N. Pacific is twice as large as that of other basins. The SH values are those for the season from July the year before to June of the year plotted. The timeline runs from 1948 or 1970 through 2005 in the NH or through June 2006 in the SH. The ACE index accounts for the combined strength and duration of tropical storms and hurricanes during a given season by computing the sum of squares of the 6-hour maximum sustained surface winds in knots while the storm is above tropical storm intensity. Adapted and updated from Levinson (2005).

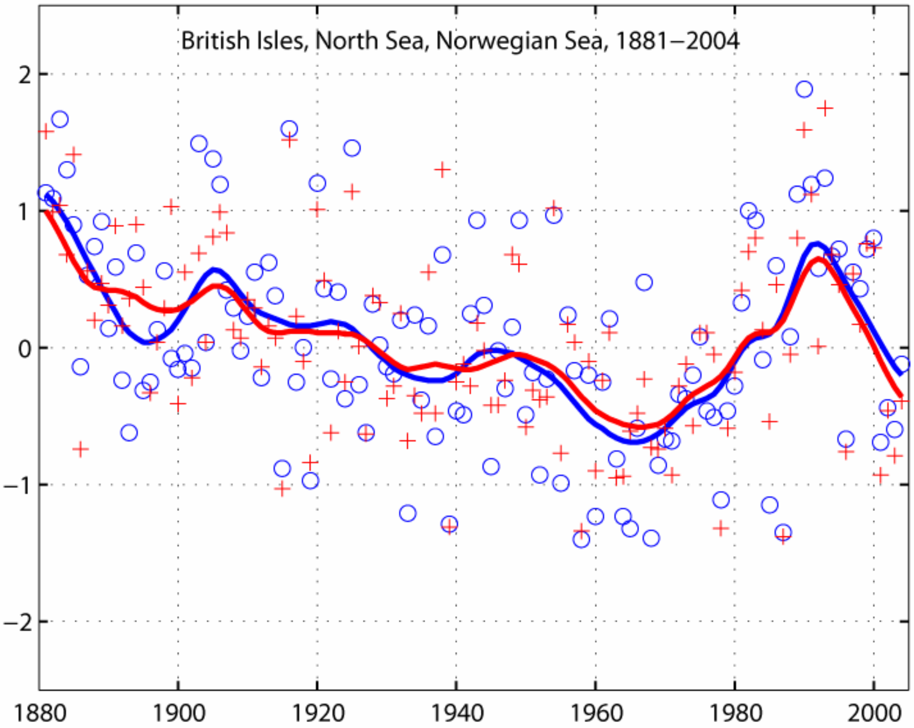

Figure 3.41. Storm index for British Isles, North Sea, Norwegian Sea, 1881 to 2004. Blue circles are 95th percentiles and red crosses 99th percentiles of standardized geostrophic winds averaged over 10 sets of triangles of stations. The smoothed curves are a decadal filter (updated from Alexandersson et al., 2000).

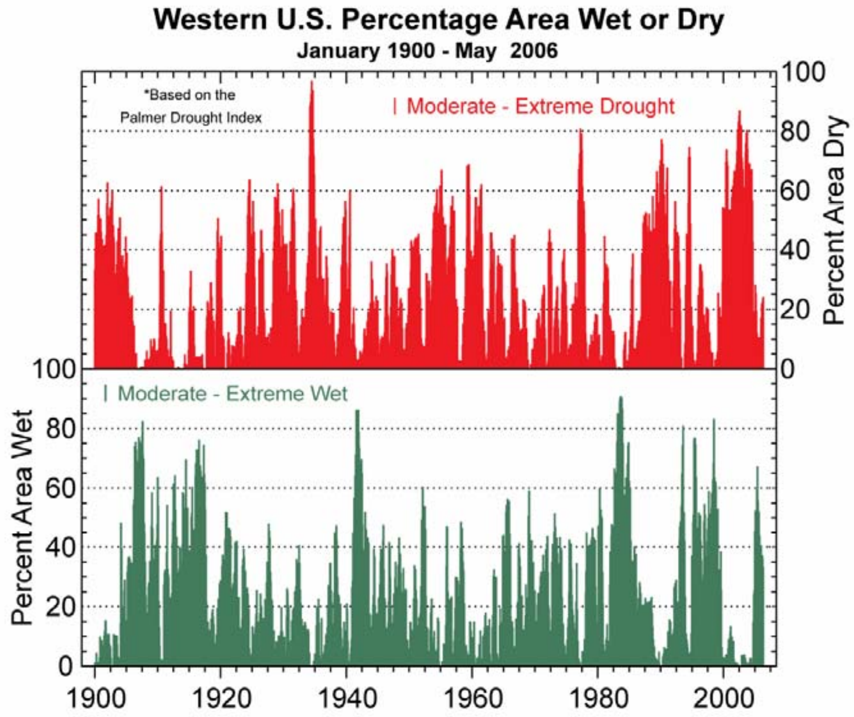

Box 3.6, Figure 1. Percentage of United States west of the Rocky Mountains (the 11 States west of and including Montana to New Mexico) dry (top) or wet (bottom) based on the Palmer Drought Severity Index for classes moderate to extreme drought or wet. From NOAA, NCDC.

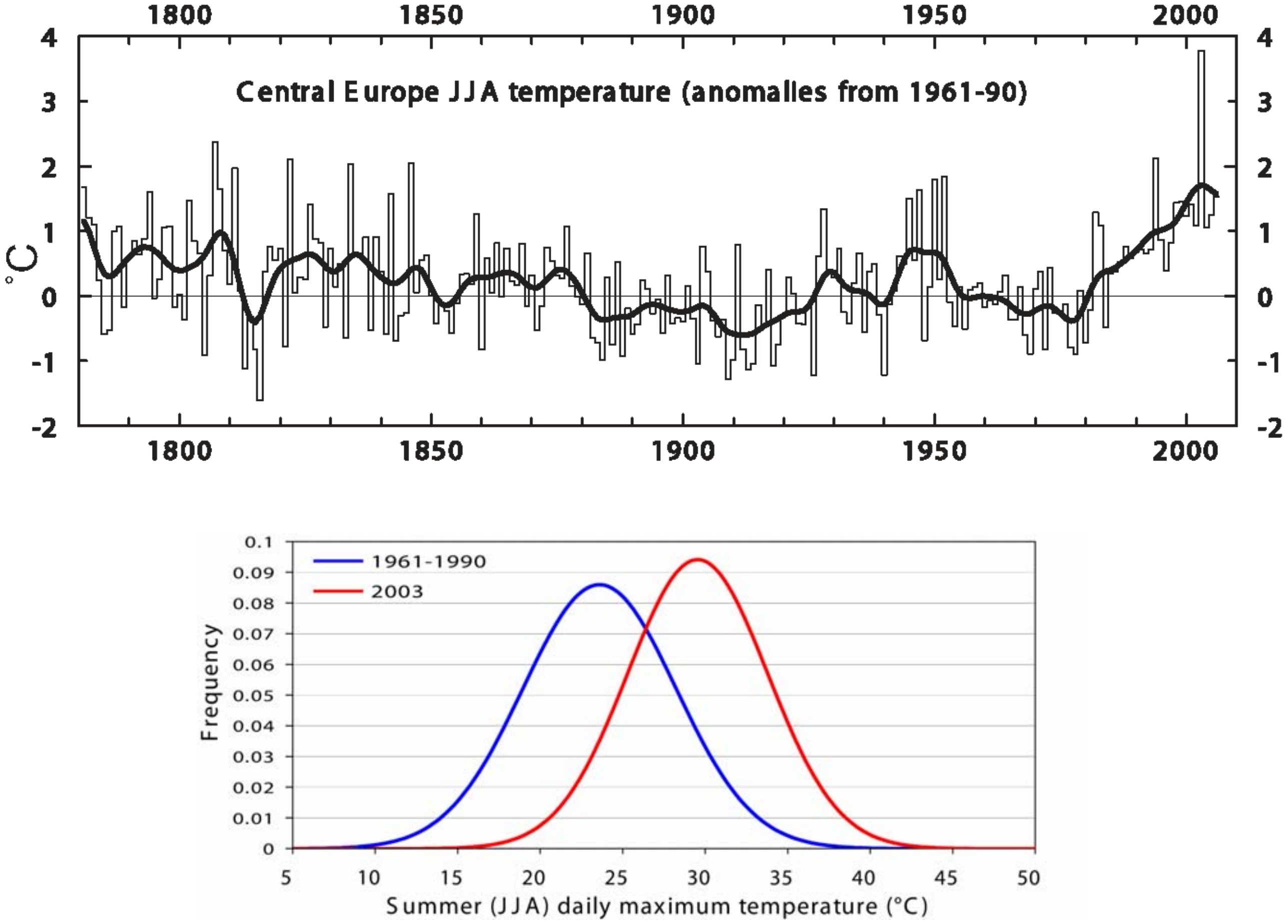

Box 3.6, Figure 2. Long time series of JJA temperature anomalies in Central Europe relative to 1961 to 1990. In the summer of 2003 the value of 3.8°C far exceeded the next largest anomaly of 2.4°C in 1807, and the highly smoothed Gaussian distribution (lower panel) of maximum temperatures (red) compared with normal (blue) at Basel, Switzerland (Beniston and Diaz, 2004) shows how the whole distribution was shifted.

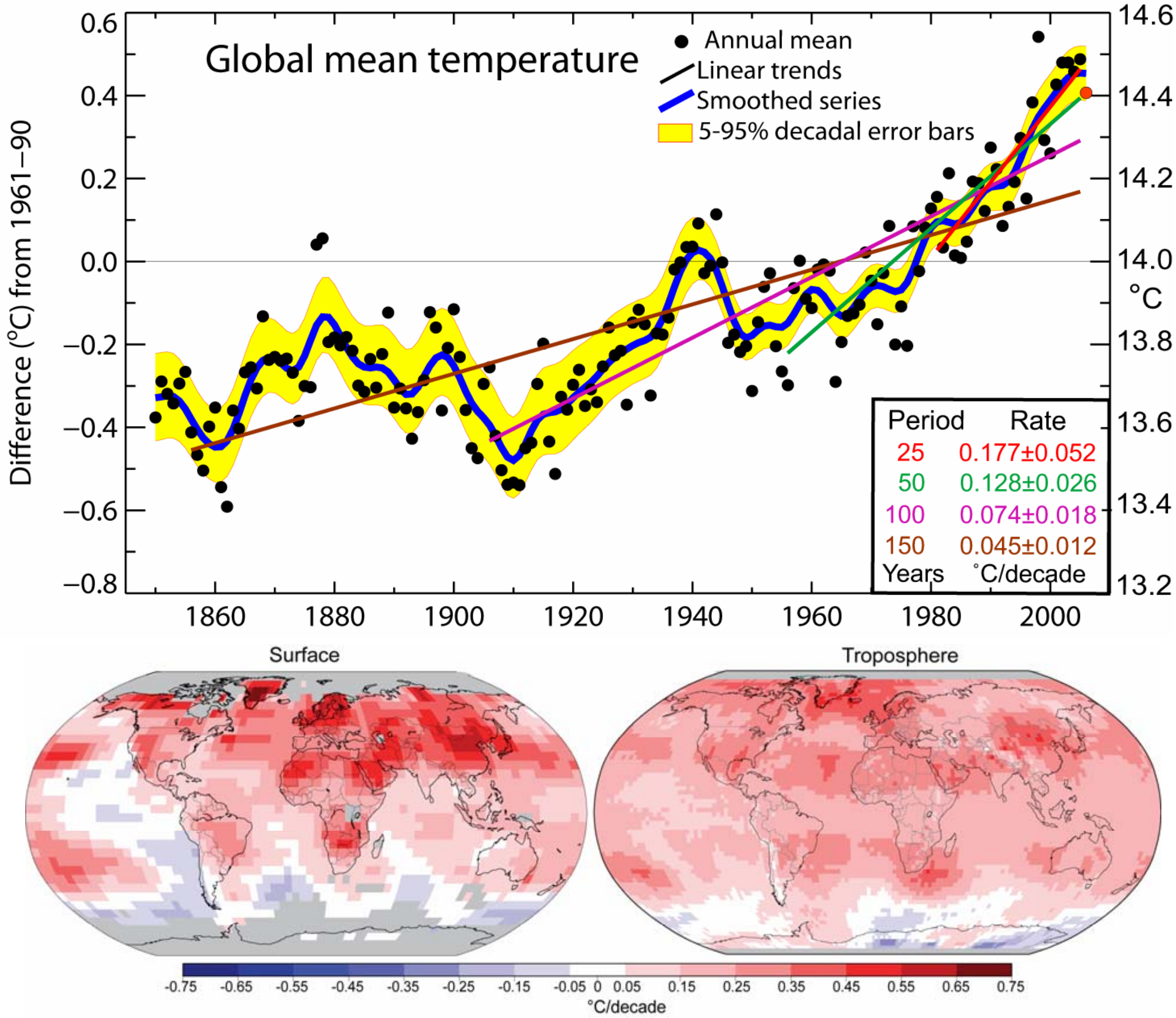

FAQ 3.1, Figure 1. *Top*: Annual global mean observed temperatures[1] (black dots) are given along with simple fits to the data. The left hand axis shows anomalies relative to a 1961 to 1990 average and the right hand axis shows the estimated actual temperature in ºC. The preliminary 2006 value is given by the orange dot. Linear trend fits to the last 25 (red), 50 (green), 100 (magenta) and 150 years (brown) are given, and correspond to 1981 to 2005, 1956 to 2005, 1906 to 2005, and 1856 to 2005. Note that for shorter recent periods, the slope is greater, indicating accelerated warming. The blue curve is a smoothed depiction to capture the decadal variations. To give an idea of whether the fluctuations are meaningful, decadal 5% to 95% (yellow) error ranges about that line are given (accordingly, annual values do exceed those limits). Results from climate models driven by estimated radiative forcings for the 20th century (Chapter 9) suggest there was little change prior to about 1915, and that a substantial fraction of the early 20th century change was contributed by naturally occurring influences including solar radiation changes, volcanism, and natural variability. From about 1940 to 1970 the increasing industrialization following World War II increased pollution in the NH contributing to cooling, and increases in carbon dioxide and other greenhouse gases dominate the observed warming after the mid-1970s. *Bottom*: Patterns of linear global temperature trends 1979 to 2005 estimated at the surface (left), and for the troposphere (from the surface to about 10 km altitude, from satellite records) (right). Grey areas indicate incomplete data. Note the more spatially uniform warming in the satellite tropospheric record while the surface temperature changes more clearly relate to land and ocean.

[1] From the HadCRUT3 dataset.

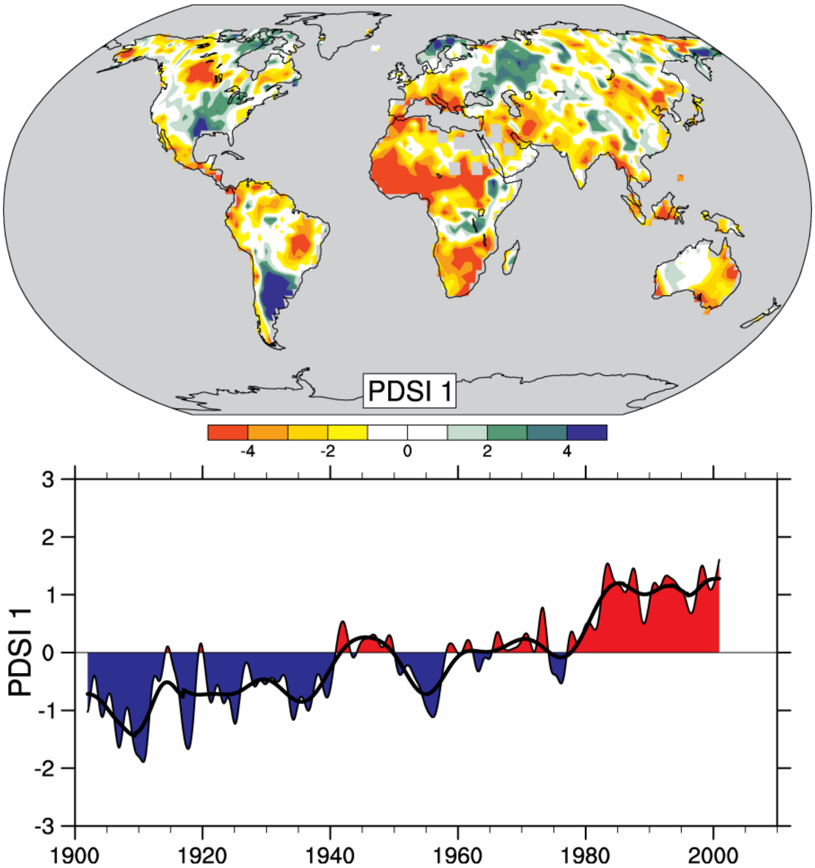

FAQ 3.2, Figure 1. The most important spatial pattern (top) of the monthly Palmer Drought Severity Index (PDSI) for 1900 to 2002. The PDSI is a prominent index of drought and measures the cumulative deficit (relative to local mean conditions) in surface land moisture by incorporating previous precipitation and estimates of moisture drawn into the atmosphere (based on atmospheric temperatures) into a hydrological accounting system. The lower panel shows how the sign and strength of this pattern has changed since 1900. Red and orange areas are drier (wetter) than average and blue and green areas are wetter (drier) than average when the values shown in the lower plot are positive (negative). The time series approximately corresponds to a trend, and this pattern and its variations account for 67% of the linear trend of PDSI from 1900 to 2002 over the global land. It therefore features widespread increasing African drought, especially in the Sahel, for instance. Note also the wetter areas, especially in eastern North and South America and northern Eurasia. Adapted from Dai et al. (2004b).

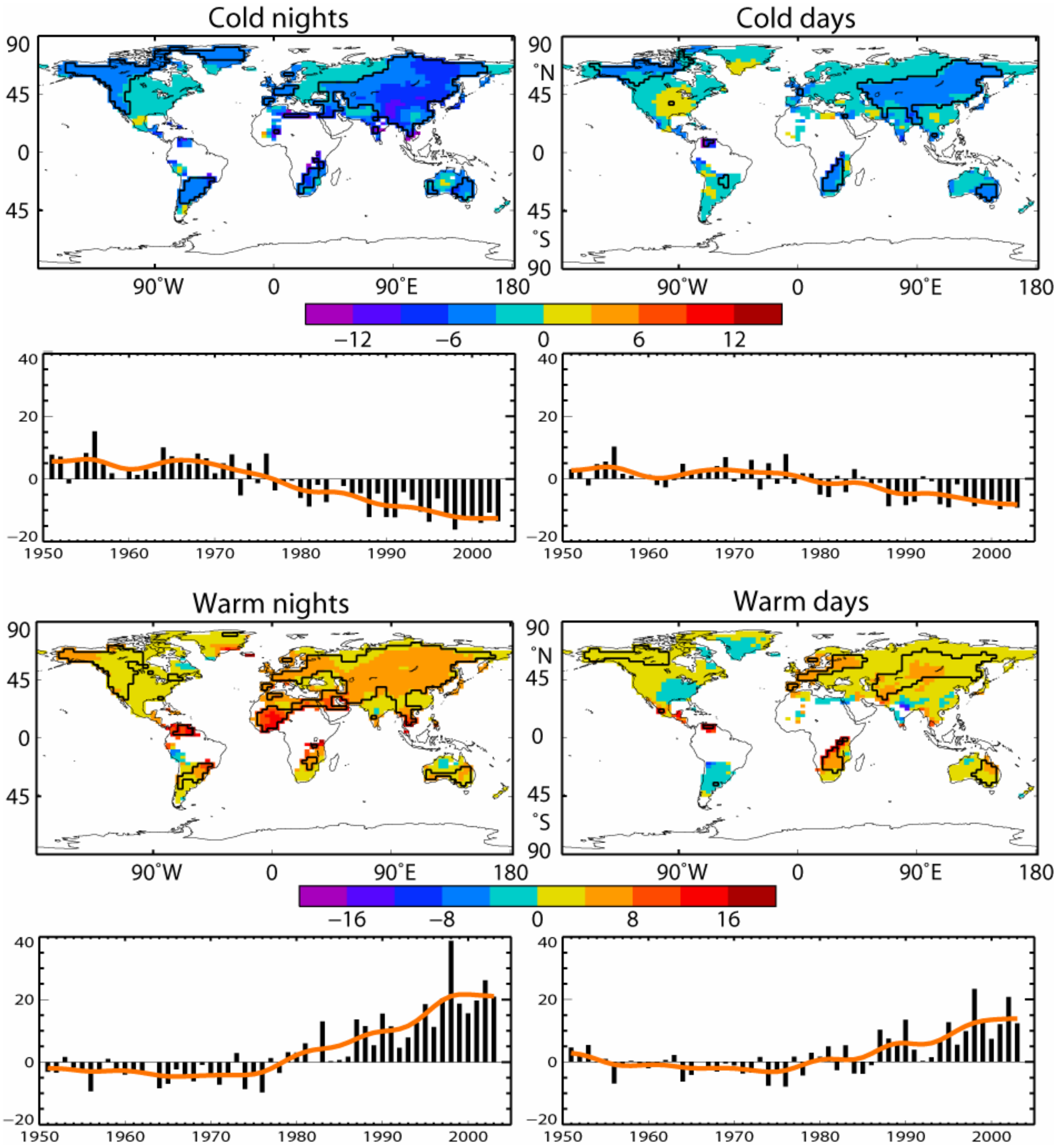

FAQ 3.3, Figure 1. The maps show observed trends (days per decade) for 1951 to 2003 in the frequency of extreme temperatures, defined based on 1961 to 1990 values, for the 10th percentile: (a) cold nights, (b) cold days; and 90th percentile: (c) warm nights, and (d) warm days. Trends were calculated only for grid boxes that had at least 40 years of data during this period and had data until at least 1999. Black lines enclose regions where trends are significant at the 5% level. Below each map are the global annual time series of anomalies (with respect to 1961 to 1990). The red line shows decadal variations. Trends are significant at the 5% level for all the global indices shown. Adapted from Alexander et al. (2006).